

Dimensional optimization of single-DOF planar rigid link-flapping mechanisms for high lift and low power

Shyam Sunder Nishad¹ and Anupam Saxena¹

¹Department of Mechanical Engineering, IIT Kanpur, India 208016.

[†] Corresponding author: shyam@iitk.ac.in

Abstract

Rigid link flapping mechanisms remain the most practical choice for flapping wing micro-aerial vehicles (MAVs) to carry useful payloads and onboard batteries for free flight due to their long-term durability and reliability. However, to achieve high agility and maneuverability—like insects—MAVs with these mechanisms require significant weight reduction. One approach involves using single-DOF planar rigid linkages, which are rarely optimized dimensionally for high lift and low power so that smaller motors and batteries could be used. We integrated a mechanism simulator based on a quasistatic nonlinear finite element method with an unsteady vortex lattice method-based aerodynamic analysis tool within an optimization routine. We optimized three different mechanism topologies from the literature. As a result, significant power savings were observed – up to 42% in some cases, due to increased amplitude and higher lift coefficients resulting from optimized asymmetric sweeping velocity profiles. We also conducted an uncertainty analysis that revealed the need for high manufacturing tolerances to ensure reliable mechanism performance. The presented unified computational tool also facilitates the optimal selection of MAV components based on the payload and flight time requirements.

Keywords: large sweeping amplitude, optimal sweeping velocity profile, rigid linkage simulator, computational tool, flapping wing MAV

1 Introduction

In the case of flapping wing micro-aerial vehicles (MAVs) with rigid linkage-based mechanisms, the weight becomes significant due to components such as motors, batteries, and flapping mechanisms. However, these mechanisms are still the most practical among all the kinds available [1–3], due to their better long-term durability and reliability when there is a need to carry some useful payload such as a camera along with an onboard battery. For flapping wing MAVs to achieve high agility, maneuverability, and hovering ability like insects, their weight should be minimized. With this idea, most insect-inspired flapping wing MAVs have focused only on the sweeping component of flapping motion, which can be implemented with planar linkages (Fig. 1). They rely on wing flexibility

for passive wing pitching, inspired by the same observed in insects [4, 5]. Incorporating active pitching motion in flapping mechanisms in the past has resulted in heavier and more complex designs suitable primarily for benchtop experiments. Stroke plane deviation is often omitted because it negatively affects lift and power consumption in most flapping patterns [6–9]. For further improvements, the single-DOF flapping mechanisms must be optimized to generate high lift and consume low power, thus allowing smaller motors and batteries while maintaining sufficient flight time.

Studies through computational fluid dynamics [10] and quasi-steady [11] aerodynamic models have shown that a larger sweeping amplitude reduces the frequency required to achieve a given lift, thus, reducing the inertial power consumption significantly [11], and consequently the overall power requirement. Larger wings can further help the rigid linkage-based flapping wing MAVs meet their high lift demands by lowering the power consumption [11]. However, such wings cannot sustain high flapping frequency and work better with larger amplitudes. In line with these observations, six-bar and seven-bar single-DOF rigid-link flapping mechanisms were proposed [12–15] that offer large sweeping amplitudes without suffering from poor force transmission quality, unlike the four-bar-based flapping mechanisms (Fig. 1). These mechanisms were optimized for a predefined large sweeping amplitude and other kinematic parameters such as symmetry between sweeping angles (and velocity profiles) of the left and right wings or symmetry of upstroke and downstroke velocity profiles, subject to constraints of no quick-return, and transmission angle of each four-bar linkages, Grashof/non-Grashof conditions. However, the effect of the sweeping velocity profile was rarely included in these optimization routines, except for Deng et al. [12] who aimed to replicate a predefined symmetric sweeping angle profile.

Wing kinematics optimization studies [17–23], using quasi-steady and unsteady aerodynamic models and experiments, have demonstrated that the mean lift and power consumption during hovering flight vary significantly depending on the sweeping velocity profiles used. This raises an important question: Should the flapping mechanisms be optimized to reproduce a sweeping velocity profile from existing studies? Two arguments challenge this idea. First, while most results agree on the mean lift trends when varying the sweeping velocity pro-

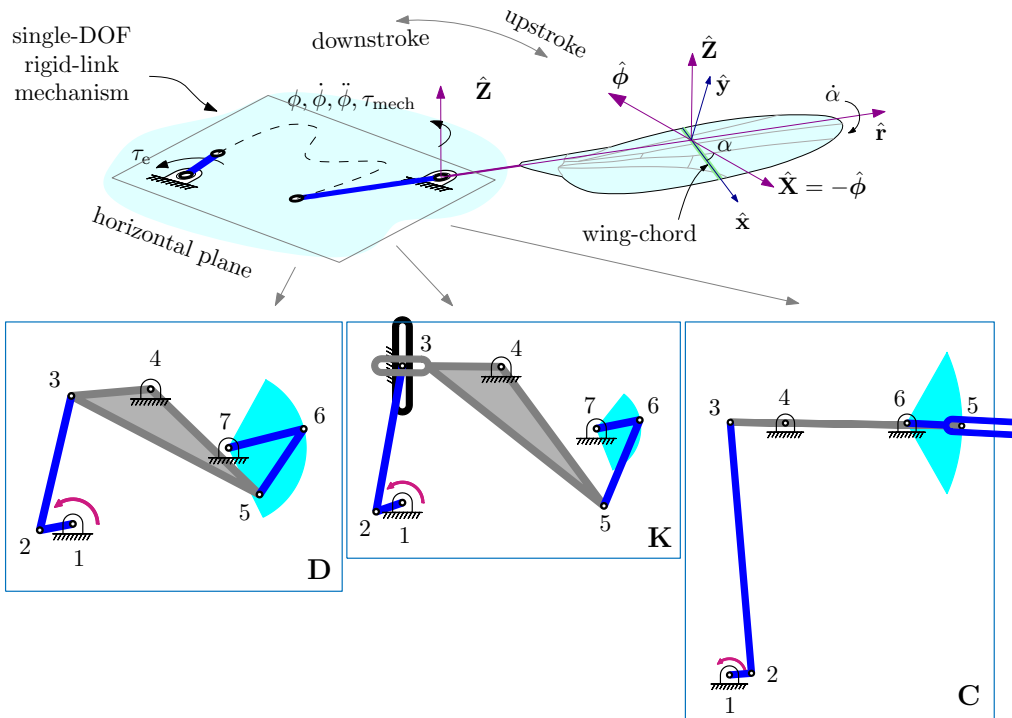


Figure 1: A single-DOF rigid-link mechanism generates the sweeping component of the flapping motion of a thin, flat, rigid wing on a horizontal plane with normal $\hat{\mathbf{Z}}$. The input torque $\tau_e \hat{\mathbf{Z}}$ results in the torque $\tau_{\text{mech}} \hat{\mathbf{Z}}$ on the output link connected to the wing whose sweeping angle, velocity, and acceleration are denoted as ϕ , $\dot{\phi}$, $\ddot{\phi}$ respectively, and the pitching angle and velocity as α and $\dot{\alpha}$ respectively. Cylindrical axes $\hat{\phi}$ and $\hat{\mathbf{Z}}$ are on the wing-chord plane $\hat{\mathbf{x}}-\hat{\mathbf{y}}$. We selected three such mechanisms from the literature for our study, that provide large amplitudes without compromising on the force transmission quality: Deng et al. [12] - denoted as D, Karásek et al. [13] - denoted as K, Coleman et al. [14] denoted as C. The configurations shown here correspond to the minimum force transmissivity index [16]. The boxes shown here are discussed in Secs. 2.1 and 3.1. Indices indicated are node numbers used in Secs. 2.1 and 2.2. The mechanisms were originally optimized for a predefined amplitude and a sinusoidal sweeping angle profile. Some research queries to be explored are: How does one know which amplitude value is optimal? Is restricting the optimization search space to symmetrical sweeping angle profiles justified?

file, there are notable disagreements on the mean power consumption trends due to differences in the aerodynamic models and the exclusion of inertial effects in some studies [18, 19, 22, 23]. Second, the sweeping velocity profiles [17] used in these studies are symmetrical about (a) the mean stroke position and (b) the two strokes. Restricting a flapping mechanism to such a symmetrical velocity profile could significantly limit the optimization search space. Notably, Terze et al. [24] attempted to address the second problem in their wing kinematics optimization study. However, they excluded aerodynamic power from their analysis, assuming that inertial power consumption was significantly higher, contradicting findings from previous studies [11, 25]. These observations suggest that instead of optimizing the mechanisms to replicate predefined kinematic parameters, optimization routines need to compute the lift and power consumption in situ by directly simulating the mechanism. This approach would enable the exploration of arbitrary sweeping velocity profiles and flapping amplitudes, unlocking greater design flexibility and potential improvements in performance.

Huang et al. [26] optimized a double crank-rocker flapping mechanism for a bird-based MAV for lift and thrust. However, they used a quasi-steady aerodynamic model that does not consider the added-mass effect, leading edge vortex effect, and wing-wake interaction. It is based on empirical coefficients, thus having limited prediction ability for optimization purposes. Han et al. [27]

optimized a single-DOF three-dimensional (3D) mechanism for sweeping and pitching motions, to generate high thrust, using the extended UVLM [28] that captures the unsteady phenomenon of vorticity shedding from the trailing edge well, along with the added mass effect, wing rotation effect, and wing wake interaction. Both of these optimizations are limited to specific mechanisms and do not compute the sweeping velocity profile generated by them.

The present work focuses on combining the computation of mechanism kinematics and aerodynamic forces into a single optimization scheme. The velocity profile is obtained from a quasistatic nonlinear finite element simulation (FEM) based on the method of truss elements by Rai et al. [29] for a generic single-DOF planar linkage with revolute joints and horizontal/vertical sliding joints extended to (i) include sliders on oscillating ternary links, and (ii) compute the mechanical advantage. Mean lift and power consumption are computed using the blade element theory coupled with a two-dimensional adaptation of the extended UVLM [28]. The leading edge vortex effect is modeled using the Polhamus leading-edge suction analogy. A multi-objective optimization is performed that maximizes mean lift and minimizes mean power consumption. The resulting Pareto set combined with a manufacturing tolerance analysis is used to select the best flapping mechanism (Fig. 4, Tab. 3). The presented unified computational tool can help make informed MAV design

decisions based on the payload and flight time requirements from a flapping wing MAV. We demonstrate these by optimizing three different topologies from the literature [12–14].

The rest of the paper is organized as follows: Sec. 2.1 lays out the optimization methodology for one-DOF planar rigid linkage flapping mechanism. A nonlinear finite element formulation for the mechanism simulator is given in Sec. 2.2, and details on the aerodynamic analysis are in Secs. 2.3 – 2.5. Section 3 presents the results, which are discussed in Sec. 4 and concluded in Sec. 5.

2 Methods

2.1 Mechanism optimization

To simulate a flapping mechanism, we assume the node 1 (Fig. 1) at the origin. Further, all link lengths are normalized with respect to crank length, such that only the ratio of other lengths is used. Therefore, node 2 is at a unit distance from the node 1. We assume a known initial orientation of the crank so that, for a mechanism with n nodes (revolute joints), we have $2n - 4$ coordinates to solve using optimization.

Using a nonlinear FEM (Sec. 2.2), we simulate the full rotation of the crank in M equal steps to obtain the rotation angles of the output link in each step as:

$$\Delta\phi_1, \Delta\phi_2, \dots, \Delta\phi_M$$

This sequence yields the output link angular velocity Ω when divided by the time Δt for each step. Assuming the crank rotating uniformly with frequency f , $\Delta t = 1/(fM)$. The output link acceleration $\dot{\Omega}$ is obtained through finite difference. Amplitude ϕ_0 can also be obtained from the above sequence. With this information about the output-link, the aerodynamic force coefficient C_F is computed using UVLM (Secs. 2.3 and 2.4), assuming a known wing pitching angle profile $\alpha(t)$. Subsequently, lift and power consumption are computed (Secs. 2.3 and 2.5). To compute the transmission quality of the mechanism (Sec. 2.2), we use the force transmissivity index (FTI) proposed by [16]. The FTI takes into account the performance of both the input and output links and is better suited for more than four link mechanisms.

We perform multiobjective optimization of the mechanism to obtain a Pareto set for maximizing lift and minimizing power consumption. For this, the following constraints are enforced:

1. link-length ratio constraint:

$$1 \leq \frac{l_{ij}}{l_{\text{crank}}} \leq r_{\text{max}}$$

such that, the crank (the input link) is the smallest one. A suitable value of r_{max} is selected to prevent very large links from being selected during optimization. The subscripts correspond to node numbers shown in Figs. 1.

2. Grashof criterion to have a crank-rocker linkage on the input side of the flapping mechanism (in absence

of crank-slider):

$$l_{12} + 2 \max\{l_{23}, l_{34}, l_{41}\} \leq l_{23} + l_{34} + l_{41} + \text{offset}$$

A small positive value of the offset (0.4: with normalized link lengths) is used to enforce Grashof's criterion strictly, to prevent the mechanism switching from one branch to another. l_{12} is the crank-length.

3. No quick return condition is imposed as an inequality constraint for optimization, with a small value of δ ($= 0.01$), since equality constraints with real numbers are not meaningful. Quick return ratio (QRR):

$$1 - \delta < \text{QRR} < 1 + \delta, \quad \text{where,}$$

$$\text{QRR} = \frac{\theta_2 - \theta_1}{2\pi - (\theta_2 - \theta_1)}$$

For the crank-rocker part of the flapping mechanisms such as D and C in Fig. 1,

$$\theta_2 = \arccos \frac{l_{34}^2 - (l_{41}^2 + (l_{23} - l_{12})^2)}{2l_{41}(l_{23} - l_{12})} + \pi$$

$$\theta_1 = \arccos \frac{l_{34}^2 - (l_{41}^2 + (l_{23} + l_{12})^2)}{2l_{41}(l_{23} + l_{12})}$$

For the crank-slider portion in the mechanism K:

$$\theta_2 = \arccos \frac{x_3}{l_{23} - l_{12}} + \pi$$

$$\theta_1 = \arccos \frac{x_3}{l_{23} + l_{12}}$$

If the input part of the mechanism is a crank-slider, we impose $x_3 = x_1 = 0$ for a vertical slider, and $y_3 = y_1 = 0$ for a horizontal slider. Thus, instead of $2n - 4$ unknowns, only $2n - 5$ need to be solved in this case.

4. large amplitude

$$\phi_{\min} \leq \phi_0 \leq \pi$$

5. the minimum value of FTI during the entire flapping cycle is the critical value FTI_{cr} . To avoid singularity and have good transmission quality, it should be high. Therefore, we impose a lower limit on this critical value as:

$$\text{FTI}_{\text{cr}} \geq \text{FTI}_{\text{min}}$$

6. box constraint: the mechanism should lie within a specified polygonal region to restrict its workspace during the entire flapping motion (Fig. 1).

2.2 One-DOF planar linkage simulator

Joints are assumed to be frictionless. To analyze a rigid linkage using the nonlinear finite element method [29], each binary link is modeled as a truss element with large axial stiffness that undergoes little strain but large rotation. A soft linear torsional spring of stiffness K_s is attached to the input link (Fig. 2(b)) whose other end is grounded. We attach a similar spring, but of high stiffness, to the output link to compute the mechanical advantage (MA, needed for FTI computation).

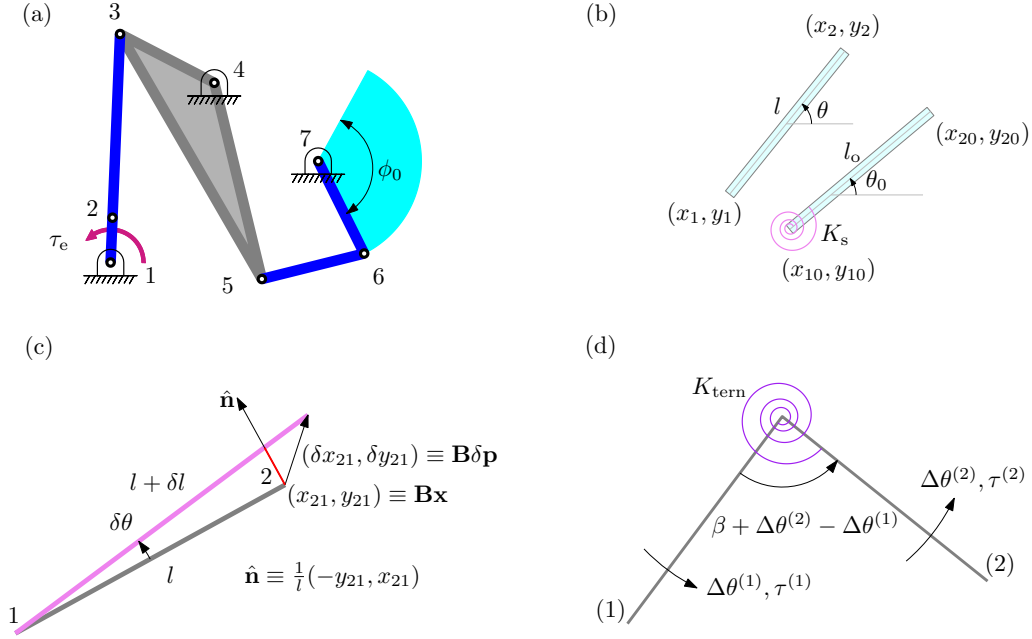


Figure 2: A single-DOF planar rigid linkage as an assembly of truss elements: (a) The nodes (revolute joints) are numbered 1,2,3, Joints are considered frictionless. A linear torsional spring with stiffness K_s (shown in (b)) is attached to one end of each link, with the other end of the spring being grounded. (b) Truss element deformation: Nodes displace from (x_{i0}, y_{i0}) to (x_i, y_i) , $i = 1, 2$ under external torque load τ_e at the actuated joint, resulting in rotation of the element by $\theta - \theta_0$ and axial deformation $l - l_0$. (c) Truss element rotation $\delta\theta$ and stretch δl due to the virtual displacement $\delta\mathbf{p}$: (x_{21}, y_{21}) and $(\delta x_{21}, \delta y_{21}) \equiv \mathbf{B}\delta\mathbf{p}$ are the current position and the virtual displacement of node 2 relative to node 1, respectively. $\hat{\mathbf{n}}$ is the normal to the current orientation of the element. Virtual displacements are arbitrarily small while applying the virtual work principle. (d) Ternary link with angle β : its two truss members (1) and (2) connected through a stiff torsional spring of stiffness K_{tern} . $\Delta\theta^{(1)}$ and $\Delta\theta^{(2)}$ correspond to the rotation of truss members from their undeformed positions (not shown here).

We simulate the mechanism in two states: (i) unlocked state in which the mechanism configuration changes and (ii) locked state in which MA is computed. In the unlocked state, we activate only the input link spring. To rotate the input link by an angle $\Delta\theta$, we apply an external torque $\tau_e = K_s\Delta\theta$ on the input link and let the system attain equilibrium quasi-statically. In the locked state, we also activate the stiff spring at the output link, which results in little rotation. Then, MA is computed as the ratio of torque developed in the output spring to the input torque. We repeat the two-state process in the successive configurations, increasing the input torque by $K_s\Delta\theta$ each time. This torque increment essentially resets the equilibrium position θ_0 of the input spring in each step ($\theta_0 = \theta_0 + \Delta\theta$: deduced from Eq. (1) by substituting $\tau_e = K_s\Delta\theta$), and the effective external load in each step remains $K_s\Delta\theta$. This effective load lets the input link rotate by $\Delta\theta$ in each step.

We implement a slider on an oscillating binary link by setting its axial stiffness to zero (e.g., link 5–6 joining nodes 5, 6 in mechanism C, Fig. 1). Using the method by Rai et al. [29], a ternary link could be implemented with three truss elements if there are only revolute joints (e.g., link 3–4–5 in mechanism D). However, if there is a slider on an oscillating ternary link (e.g., link 3–4–5 in mechanism K), lengths of the truss members connected to the slider vary freely because of its zero axial stiffness (like the members 3–4, 3–5), thus, adding an extra DOF and rendering the existing method incapable. Hence, we proposed a new method for such cases.

To derive the element force vectors and element tan-

gent stiffness matrices, we use the virtual work principle. Given the nodal positions $\mathbf{x}_0 = [x_{10} \ y_{10} \ x_{20} \ y_{20}]^T$ of a truss element in an equilibrium configuration, we need to find the new equilibrium position $\mathbf{x} = [x_1 \ y_1 \ x_2 \ y_2]^T$, when external load torque τ_e is applied (Fig. 2(b)). The virtual work residual of the internal and external forces can be written as:

$$\mathbf{g} \cdot \delta\mathbf{x} = \underbrace{\int \sigma \delta\epsilon \, dV}_{\text{on truss element}} + \underbrace{K_s(\theta - \theta_0)\delta\theta}_{\text{on spring}} - \underbrace{\tau_e \delta\theta}_{\text{by external load}} \quad (1)$$

where, σ is the stress in the element due to the displacement $\mathbf{x} - \mathbf{x}_0$ during which the element rotates from initial orientation θ_0 to θ . $\delta\epsilon$ is the strain due to the virtual displacement $\delta\mathbf{x}$. $\delta\theta$ is the corresponding rotation of the element. Assuming uniform small strain and volume conservation ($V = l_0 A_0 = lA$), we obtain:

$$\int \sigma \delta\epsilon \, dV = (E\epsilon)\delta\epsilon(l_0 A_0) = EA_0 \frac{l - l_0}{l_0} \delta l = G \frac{l - l_0}{l_0} \delta l \quad (2)$$

where, E is the Young's elasticity modulus, l_0 and l are the original and deformed lengths, A_0 and A are the corresponding cross-sectional areas, and $EA_0 = G$ (axial stiffness). From Fig. 2(c):

$$l^2 = [x_{21} \ y_{21}] \begin{bmatrix} x_{21} \\ y_{21} \end{bmatrix} = \mathbf{x}^T (\mathbf{B}^T \mathbf{B}) \mathbf{x} \Rightarrow \delta l = \frac{1}{l} \mathbf{y}^T \delta \mathbf{x} \quad (3)$$

where,

$$\begin{bmatrix} x_{21} \\ y_{21} \end{bmatrix} = \begin{bmatrix} x_2 - x_1 \\ y_2 - y_1 \end{bmatrix} = \underbrace{\begin{bmatrix} -1 & 0 & 1 & 0 \\ 0 & -1 & 0 & 1 \end{bmatrix}}_{\mathbf{B}} \mathbf{x}, \quad \mathbf{y} = (\mathbf{B}^T \mathbf{B}) \mathbf{x}$$

From Fig. 2(c), we can compute the virtual rotation $\delta\theta$ as:

$$\delta\theta = \frac{\hat{\mathbf{n}} \cdot \mathbf{B}\delta\mathbf{x}}{l} = \frac{1}{l^2} [-y_{21} \quad x_{21}] \mathbf{B}\delta\mathbf{x} = \frac{1}{l^2} \mathbf{z}^T \delta\mathbf{x} \quad (4)$$

where,

$$\mathbf{z} = \mathbf{B}^T \begin{bmatrix} -y_{21} \\ x_{21} \end{bmatrix} = \mathbf{B}^T \underbrace{\begin{bmatrix} 0 & 1 & 0 & -1 \\ -1 & 0 & 1 & 0 \end{bmatrix}}_{\mathbf{c}} \mathbf{x}$$

Substituting in Eq. (1) from Eqs. (2)–(4), and invoking arbitrariness of the virtual displacement $\delta\mathbf{x}$, we obtain:

$$\mathbf{g}(\mathbf{x}) = a\mathbf{y} + b\mathbf{z} \quad (5)$$

From this equation, the tangent stiffness matrix \mathbf{K}_t for the element can be obtained as:

$$\mathbf{K}_t = \frac{\partial \mathbf{g}}{\partial \mathbf{p}} = c\mathbf{y}\mathbf{y}^T + a\mathbf{B}^T \mathbf{B} + b\mathbf{B}^T \mathbf{c} - e\mathbf{z}\mathbf{y}^T + d\mathbf{z}\mathbf{z}^T \quad (6)$$

where,

$$\begin{aligned} a &= \frac{G}{l} \frac{l - l_0}{l_0}, & b &= \frac{K_s(\theta - \theta_0) - \tau_e}{l^2}, \\ c &= \frac{G}{l^3}, & d &= \frac{K_s}{l^4}, & e &= \frac{2b}{l^2} \end{aligned} \quad (7)$$

A ternary link is implemented with two truss members with a stiff linear torsional spring of stiffness K_{tern} between them (Fig. 2(d)). The high stiffness of this spring ensures that the angle β between the two members changes very little. As the truss members deflect by angles $\Delta\theta^{(1)}$ and $\Delta\theta^{(2)}$ from their undeformed positions, they experience the torque $\tau^{(1)}$ and $\tau^{(2)}$ respectively due to this spring:

$$\tau^{(1)} = -K_{\text{tern}} (\Delta\theta^{(1)} - \Delta\theta^{(2)}), \quad \tau^{(2)} = -K_{\text{tern}} (\Delta\theta^{(2)} - \Delta\theta^{(1)})$$

Superscripts (1) and (2) correspond to the truss members 1 and 2 of the ternary link. Thus, the virtual work equation in Eq. (1) for these two members gets modified to:

$$\begin{aligned} \mathbf{g}^{(1)} \cdot \delta\mathbf{x}^{(1)} &= \int \sigma^{(1)} \delta\epsilon^{(1)} dV + (K_s \Delta\theta^{(1)} - \tau_e^{(1)}) \delta\theta^{(1)} \\ &\quad + K_{\text{tern}} (\Delta\theta^{(1)} - \Delta\theta^{(2)}) \delta\theta^{(1)} \\ \mathbf{g}^{(2)} \cdot \delta\mathbf{x}^{(2)} &= \int \sigma^{(2)} \delta\epsilon^{(2)} dV + (K_s \Delta\theta^{(2)} - \tau_e^{(2)}) \delta\theta^{(2)} \\ &\quad + K_{\text{tern}} (\Delta\theta^{(2)} - \Delta\theta^{(1)}) \delta\theta^{(2)} \end{aligned}$$

The spring K_s and external torque τ_e are retained for generality. Solutions are similar to Eq. (5), but depend on the nodal positions of both members, due to coupling through the stiff spring.

$$\begin{aligned} \mathbf{g}^{(1)}(\mathbf{x}^{(1)}, \mathbf{x}^{(2)}) &= a^{(1)} \mathbf{y}^{(1)} + b^{(1)} \mathbf{z}^{(1)} + b'^{(1)} \mathbf{z}^{(1)} \\ \mathbf{g}^{(2)}(\mathbf{x}^{(1)}, \mathbf{x}^{(2)}) &= a^{(2)} \mathbf{y}^{(2)} + b^{(2)} \mathbf{z}^{(2)} + b'^{(2)} \mathbf{z}^{(2)} \end{aligned}$$

Thus, we obtain tangent stiff matrix terms for the truss member 1 from both $\frac{\partial \mathbf{g}^{(1)}}{\partial \mathbf{x}^{(1)}}$ and $\frac{\partial \mathbf{g}^{(1)}}{\partial \mathbf{x}^{(2)}}$, where,

$$\begin{aligned} \frac{\partial \mathbf{g}^{(1)}}{\partial \mathbf{x}^{(1)}} &= c^{(1)} \mathbf{y}^{(1)} \mathbf{y}^{(1)T} + a^{(1)} \mathbf{B}^T \mathbf{B} + (b^{(1)} + b'^{(1)}) \mathbf{B}^T \mathbf{c} \\ &\quad - (e^{(1)} + e'^{(1)}) \mathbf{z}^{(1)} \mathbf{y}^{(1)T} + (d^{(1)} + d'^{(1)}) \mathbf{z}^{(1)} \mathbf{z}^{(1)T} \end{aligned} \quad (8)$$

$$\frac{\partial \mathbf{g}^{(1)}}{\partial \mathbf{x}^{(2)}} = -\frac{K_{\text{tern}}}{l^{(1)2} l^{(2)2}} \mathbf{z}^{(1)} \mathbf{z}^{(2)T} \quad (9)$$

The expressions for $a^{(1)}$, $a^{(2)}$, $b^{(1)}$, $b^{(2)}$, $c^{(1)}$, $c^{(2)}$, $d^{(1)}$, $d^{(2)}$ are obtained from Eq. (7) by substituting values for the respective truss members, whereas,

$$\begin{aligned} b'^{(1)} &= \frac{K_{\text{tern}}}{l^{(1)2}} (\Delta\theta^{(1)} - \Delta\theta^{(2)}), & b'^{(2)} &= \frac{K_{\text{tern}}}{l^{(2)2}} (\Delta\theta^{(2)} - \Delta\theta^{(1)}) \\ d'^{(1)} &= \frac{K_{\text{tern}}}{l^{(1)4}}, & e'^{(1)} &= \frac{2b'^{(1)}}{l^{(1)2}} \end{aligned}$$

Tangent stiffness matrix terms for the truss member 2 can be obtained by interchanging indices 1 and 2 in Eqs. (8) and (9).

In indicial notation, the terms of global tangent stiffness matrix can be written as:

$$K_{ij} = \frac{\partial g_i}{\partial x_j}, \quad \text{since, } \delta g_i = \frac{\partial g_i}{\partial x_j} \delta x_j = K_{ij} \delta x_j$$

When assembling element tangent stiffness matrices $\frac{\partial \mathbf{g}}{\partial \mathbf{x}}$ to form the global tangent stiffness matrix K_{ij} , the terms from $\frac{\partial \mathbf{g}}{\partial \mathbf{x}}$ go in the rows corresponding to the global DOFs of the element whose force residual vector \mathbf{g} is used, and in columns corresponding to the global DOFs of the element whose position vector \mathbf{x} is used. Thus, in the case of ternary links, $\frac{\partial \mathbf{g}^{(1)}}{\partial \mathbf{x}^{(1)}}$ corresponds to global DOFs from the truss member 1 alone. But, in case of $\frac{\partial \mathbf{g}^{(1)}}{\partial \mathbf{x}^{(2)}}$, the rows correspond to those from truss member 1, while columns to the truss member 2. Similarly, the element stiffness matrices $\frac{\partial \mathbf{g}^{(2)}}{\partial \mathbf{x}^{(2)}}$ and $\frac{\partial \mathbf{g}^{(2)}}{\partial \mathbf{x}^{(1)}}$ for the truss member-2 of the ternary link, are assembled. Once the global stiffness matrix and global force residual vector are formed, Newton Raphson method is used to solve for the nodal positions \mathbf{x} , after removing their rows and columns corresponding to the fixed DOFs, as usual.

We compute the force transmissivity index (FTI) as [16]:

$$\text{FTI} = |\text{MA} \times \text{EFR}|$$

where, MA is the mechanical advantage of the linkage. EFR, the effective force ratio, is the ratio of power flowing in the output link from the input side of the mechanism to the maximum power that can flow from the same side. In case there is only one link connected to the output link from the input side, as in Fig. 2 and the output link is connected to the ground,

$$\text{EFR} = \sin \gamma = \frac{g_2 x_{21} - g_1 y_{21}}{\sqrt{g_1^2 + g_2^2} \sqrt{x_{21}^2 + y_{21}^2}}$$

where, γ is the angle between the output link and the force (g_1, g_2) applied by the connected link on the output link. Here, the vector (x_{21}, y_{21}) gives the orientation of the output link (Fig. 2C). The internal force (g_1, g_2) is obtained from the 4×1 element force vector \mathbf{g} corresponding to the connected link with the output spring active. The mechanical advantage is obtained as:

$$MA = \frac{K_{\text{out}}\Delta\phi}{\tau_e}$$

where, $\Delta\phi$ is the output link rotation computed during the locked-state in each configuration. K_{out} is the stiffness of the output spring.

2.3 Aerodynamic model

For the aerodynamic analysis, we use blade element theory to divide the wing into thin chords and analyze a wing chord using the 2D unsteady vortex lattice method (UVLM). UVLM is based on the potential flow theory and provides a good balance between computational cost and accuracy. It cannot inherently model the leading edge separation (LEV) and viscous effects. However, it captures the unsteady phenomenon of vorticity shedding from the trailing edge well, along with the added mass effect, wing rotation effect, and wing wake interaction. Dickinson et al. [30] showed experimentally that the aerodynamic forces in hovering flapping wing motion are roughly normal to the wing, indicating that viscosity affects majorly in structuring vorticity around the wing rather than the aerodynamic forces. Persson et al. [31] demonstrated through numerical simulations that the potential theory-based numerical solvers can give the correct trend of forces when flow separated at leading edge reattaches and is suitable for preliminary design purposes. Ansari et al. [32, 33] modeled vorticity shedding from both leading and trailing edges in their 2D discrete vortex model based on potential theory. However, their approach is computationally costlier than UVLM, as it involves solving two nonlinear integral equations compared to a system of linear equations in UVLM, thus prohibiting its use in optimization problems due to a large number of function evaluations. Rocca et al. [34] included vorticity shedding from both leading and trailing edges in UVLM. However, that presented numerical instabilities due to wing-wake interaction in hovering. Therefore, Nguyen et al. [28] incorporated the LEV effect through Polhamus leading-edge suction analogy along with a vortex core growth model for wake vortices to address this problem and validated UVLM results against CFD and experimental data. Wang et al. [35] reported that the unsteady force estimates from 2D CFD computations are not much different from experiments because insects reverse their strokes before a leading edge vortex would shed in a corresponding 2D wing motion. In light of the above evidences, we chose the extended UVLM formulation by Nguyen et al. [28] for our aerodynamic analysis but traded off the improved accuracy of 3D computations for higher computation speed with its 2D-variant.

A brief summary of the 2D UVLM is given in Fig. 3a, and more details can be found in App. A and Ref. [36].

The nondimensional 2D-UVLM yields the force coefficient C_F for 2D motion of wing-chord given by nondimensional sweeping velocity $\tilde{\Omega}(\tilde{t})$ and pitching angle $\alpha(\tilde{t})$, where \tilde{t} is the nondimensional time. In inviscid flow, the force coefficient C_F remains the same for all the wing chords of the finite wing, neglecting the tip effect. Therefore, using blade element theory, the lift for a finite wing of length R (surface area S) and second moment of area r_2 , flapping at frequency f is obtained as:

$$L = C_L \frac{\rho}{2} \Omega_{\text{ref}}^2 r_2^2 S = C_L \frac{\rho}{2} \Omega_{\text{ref}}^2 \hat{r}_2^2 R^2 S \quad (10)$$

where, $\hat{r}_2 = r_2/R$ is the nondimensional second moment of area. The aerodynamic torque in the plane of the motion of the mechanism, assuming horizontal stroke plane, is computed from the horizontal force:

$$\tau_{\text{aero}} = \int r \hat{\mathbf{r}} \times C_H \frac{\rho}{2} \Omega_{\text{ref}}^2 r^2 dS \hat{\phi} = C_H \frac{\rho}{2} \Omega_{\text{ref}}^2 r_3^3 S \dot{\mathbf{Z}}$$

where, r_3 is the third moment of the wing area, lift coefficient $C_L = C_F \cos \alpha$, horizontal force-coefficient $C_H = -C_F \sin \alpha$, and $\Omega_{\text{ref}} = 2\phi_0 f$, ϕ_0 being the sweeping amplitude, and ρ , the fluid density (App. A).

2.4 Force due to LEV

We use the Polhamus leading-edge suction analogy [37] to estimate the force due to the leading edge vortex (LEV). According to this analogy, the force due to the leading edge vortex in a separated flow is equal in magnitude to the suction force if the flow remains attached. However, the direction of the force in a separated flow is rotated normally to the wing chord. Therefore, this force coefficient C_{LES} is added to the normal force coefficient C_F , when the angle of attack α is greater than a critical value α_c , above which the leading edge separation occurs (Fig. 3c).

$$C_{F,\text{net}} = C_F + \text{sign}(\cos \alpha) |C_{\text{LES}}|$$

When $\alpha < \alpha_c$, no separation occurs. Hence, C_{LES} is parallel to the wing-chord, directed towards the leading edge, and added vectorially to $C_F \hat{\mathbf{y}}$. In this paper, $\alpha_c = 12$ deg is taken, similar to that by Nguyen et al. [28] and Rocca et al. [34]. It is also noted that the derivation presented here considers only the steady terms in the Blasius equation. During the rotation phase of the flapping motion, the role of LEV becomes less significant compared to the rotational effects. Hence, the error due to the exclusion of unsteady terms may not be significant (similar assumption in [28]); Rocca et al. [34] do not use a suction model as they consider shedding of vortices from both the leading and trailing edges).

To derive the leading edge suction force, we apply the steady Blasius theorem around a closed loop C of infinitesimal radius around the leading edge of the wing chord. To justify the use of this theorem, we make the following assumptions. The flow velocity \mathbf{u} relative to the wing chord can be decomposed as:

$$\mathbf{u} = \mathbf{q} + \mathbf{u}_{\text{LE}}^b$$

where, \mathbf{u}_{LE}^b is the flow velocity due to singularity at the leading edge, and \mathbf{q} is the velocity relative to the wing-chord due to all other causes (wing-chord motion, wake

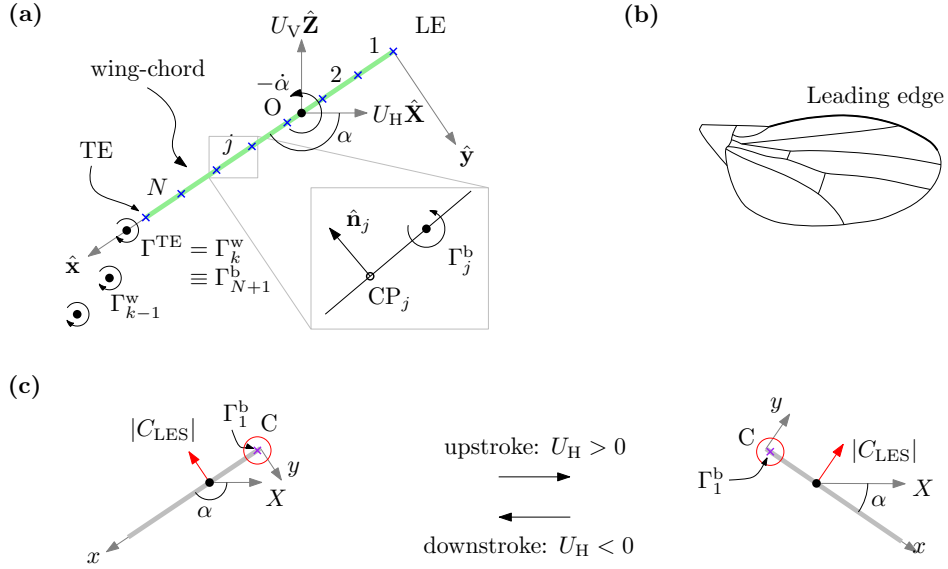


Figure 3: Aerodynamic model: **(a)** 2D-UVLM: A thin, flat, rigid wing-chord with orientation α relative to the horizontal (Fig. 1), translates with velocity $U_H \hat{\mathbf{X}}$, and deviates from the horizontal stroke plane with velocity $U_V \hat{\mathbf{Z}}$. It also rotates with velocity $\dot{\alpha} \hat{\mathbf{r}}$ about O. Due to the wing motion, a bound circulation develops around the wing chord. In 2D UVLM, the wing-chord is split into N panels (elements) of length d each, numbered $1, 2, \dots, j, \dots, N$. Using the lumped vorticity model [36], circulation Γ_j^b in each panel is placed at $d/4$ from the end towards the leading edge LE. No-penetration condition is imposed at $3d/4$ (collocation points CP_j) from the same end. A trailing edge vortex (TEV) with circulation $\Gamma^{\text{TE}} (\equiv \Gamma_{N+1}^b)$: notation) is assumed bound at a distance $d/4$ from the trailing edge TE, which sheds into the wake at each time instant. Γ_k^w is the TEV shed at the k^{th} time step t_k ($k = 1$: the initial step). That means, for analysis at t_k , there are $N_w = k - 1$ vortices in the wake, and $\Gamma_k^w = \Gamma^{\text{TE}}$ is still bound. The TEV and all wake vortices are transported with the flow, retaining their circulations constant at all times, as per Kirchoff's equation of motion of free vortices. Total circulation ($\sum_{j=1}^{N+1} \Gamma_j^b + \sum_{i=1}^{N_w} \Gamma_i^w$) is conserved at each time instant as per Kelvin's theorem. **(b)** Fruit fly wing for force computations: A simplified design is considered for inertial force computation: The skeleton is assumed to be made of solid carbon fiber rods of 0.8 mm diameter. Six straight rods of length equal to the wing length and two small rods of length $\frac{1}{5}$ of the mean wing chord are assumed to make the skeleton. To simplify computations, the mass in these rods is uniformly distributed over the entire wing-surface area. The wing membrane is assumed to be made of a mylar sheet of 10 microns thick. **(c)** Leading edge vortex (LEV) force using the Polhamus leading-edge suction analogy: Since the LEV exists only on the upper side of the wing chord throughout the translation phase, the force is always directed upwards. C is the contour loop centered at the leading edge panel vortex Γ_1^b , used to compute the LES force using the Blasius theorem.

vortices, and bound vortices except the singularity at the leading edge LE). The velocity \mathbf{q} can be considered to be uniform and much less than that due to the LE singularity. This means we can compute \mathbf{q} at the center of the loop and use it at all points on the curve C. In 2D-UVLM, the bound vortex in the leading edge panel can be considered as the LE singularity. Therefore, the loop C is centered around this singularity (Fig. 3c.) Thus, from Biot-Savart law (used in Eq. (17)),

$$\mathbf{u}_{\text{LE}}^b = \frac{\Gamma_1^b}{2\pi} \frac{\hat{\mathbf{k}} \times (\mathbf{r} - \mathbf{r}_1^b)}{\|\mathbf{r} - \mathbf{r}_1^b\|^2}$$

we obtain the velocity at a point \mathbf{r} on the curve C. Γ_1^b is the circulation in the leading edge panel ($j = 1$). With the assumption $\|\mathbf{q}\| \ll \|\mathbf{u}_{\text{LE}}^b\|$, we can assume the curve C to be a streamline, and thus, make the Blasius theorem applicable. In complex notation,

$$u = q + \frac{\Gamma_1^b}{2\pi i (z - z_1^b)} \quad (11)$$

where, in the standard notations, $u = u_x - i u_y$, $q = q_x - i q_y$ (subscripts x and y denote x and y components).

Invoking the Blasius theorem,

$$F_x - i F_y = \oint_C \frac{i\rho}{2} u^2 dz$$

Substituting from Eq. (11) and using the assumption of uniform q , the above integral yields:

$$F_x = \rho q_y \Gamma_1^b, \quad F_y = -i \rho q_x \Gamma_1^b$$

Note that F_y is already included in the force computed in UVLM from Eq. (20). F_x is the leading edge suction force. This can be nondimensionalized to obtain the corresponding force coefficient as:

$$C_{\text{LES}} = \frac{F_x}{\frac{1}{2} U_{\text{ref}}^2 \bar{c}} = 2\bar{q}_y \Gamma_1^b$$

2.5 Computation of inertial torque and power

We consider a fruit fly wing planform for our aerodynamic computations and use a simplified structure of the wing for inertial power computation, as detailed in Fig.

3b. If the sweeping acceleration is $\dot{\Omega}$, the inertial torque on the wing can be written as:

$$\tau_{\text{inertial}} = I\dot{\Omega}, \quad I = \rho_w S t_w r_2^2$$

where, I is the mass moment of inertia of the wing with second moment of area r_2 , $S = R^2/r_a$ being the wing-surface area, R , r_a , t_w and ρ_w – length, aspect-ratio, thickness and density of the wing respectively. The wing-density ρ_w is estimated by adding contribution of mass m_c of wing-skeleton formed from carbon-fiber rods (distributing uniformly over wing-area) to the wing membrane density ρ_{mylar} :

$$\rho_w = \frac{m_c}{S t_w} + \rho_{\text{mylar}}, \quad m_c = l_c \pi r_c^2 \rho_c, \quad l_c = 6R + \frac{2R}{5 r_a}$$

where, l_c is the total length of the carbon fiber rods with diameter r_c and density ρ_c .

We can write the equation of motion of the wing actuated by the output link of the flapping mechanism as:

$$\tau_{\text{aero}} + \tau_{\text{mech}} = \tau_{\text{inertial}}$$

where, τ_{aero} is the aerodynamic torque on the wing, τ_{mech} is the torque applied by the mechanism on the wing to execute the required wing kinematics. Thus, the power consumed by the wing motion is given by:

$$P_{\text{mech}} = \tau_{\text{mech}} \Omega = \rho \Omega_{\text{ref}}^3 R^3 S \left(\frac{\rho_w}{\rho} \tilde{t}_w \hat{r}_2^3 \tilde{\Omega}' - \frac{C_H}{2} \hat{r}_3^3 \right) \tilde{\Omega} \quad (12)$$

Here, $\tilde{t}_w = t_w/L_{\text{ref}}$ is the nondimensional wing-thickness (L_{ref} : mean chord length), $\hat{r}_3 = r_3/R$ is the nondimensional third moment of wing-area, and $\tilde{\Omega}'$ is the nondimensional sweeping acceleration. In the above formulation, we have excluded the inertial power consumed by the flapping mechanism (Sec. 4).

3 Results

We selected three flapping mechanism topologies (Fig. 1) from the literature to investigate whether optimizing them dimensionally for predefined kinematic parameters such as sweeping amplitudes and sweeping angle profiles is justified. These mechanisms can provide large sweeping amplitudes (≥ 120 deg) without compromising force transmission quality. The topologies used by Deng et al. [12], Karásek et al. [13], and Coleman et al. [14] are referred to here as D, K, and C respectively. The wing sweeping velocity profiles were generated using the mechanism simulator and used to evaluate lift and power consumption using 2D-UVLM during the multiobjective optimization which maximized the lift and minimized the power consumption to yield a Pareto set for each mechanism topology. Finally, we analyzed the Pareto solutions for manufacturing tolerances to select the best solution.

Before optimization, we conducted a convergence study of the 2D-UVLM and validated the method against the experimental data from literature by simulating fruit fly, oval, and figure-8 flapping wing kinematics. To balance computation time with convergence, we chose number of lattice elements $N = 40$ and $N_t = 4$ for all our simulations, where N_t is defined such that the nondimensional

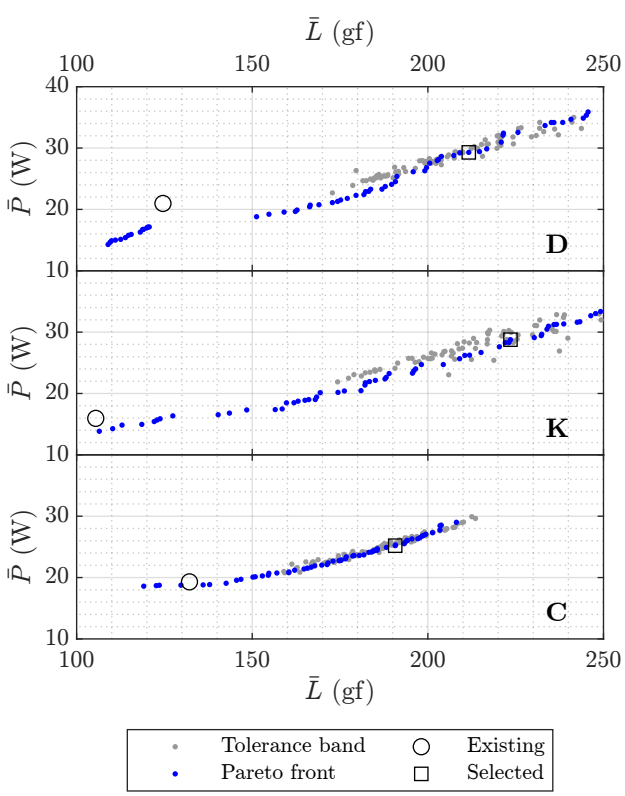
time step $\delta \tilde{t} = \frac{\tilde{d}/\tilde{\Omega}_{\text{max}}}{N_t}$, and $N_t = 1$ yields the time for the lattice element to move by one element length \tilde{d} with velocity $\tilde{\Omega}_{\text{max}}$. We observed that for Squire's parameter $a = 10^{-4}$, convergence was achieved in all cases considered in this study. Details are provided in the supplementary material.

We found that the singularity percentage, i.e., the number of quasi-random linkages having singular configurations out of the 100, hovered between 10 to 50 for the mechanisms D and K and zero for the mechanism C. The number of non-singular quasi-random linkages violating the FTI_{min} constraint lied between 5 to 50 for mechanisms D and K, and 0 to 50 for mechanism C. Further, the number of nonsingular quasi-random linkages violating the relaxed amplitude constraint (<100 deg) lied between 0 to 25 for mechanism D, whereas it was close to zero for the other two mechanisms.

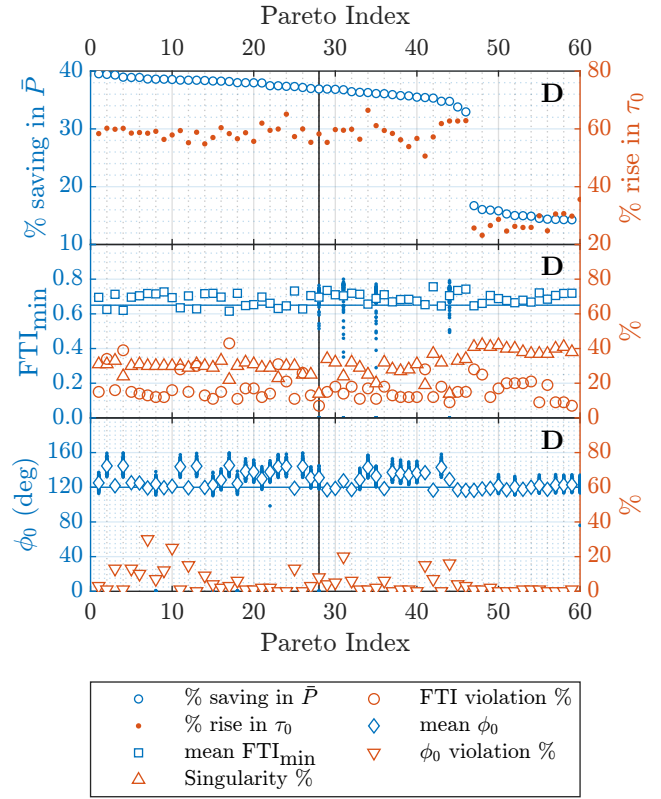
3.1 Optimization constraints and parameters

For the multiobjective optimization, all six constraints were imposed. The minimum amplitude was set to 120 deg. The boxes used for the box constraint are shown in Fig. 1, and each corresponds to a rectangular boundary that encloses the workspace and the mechanism with the existing dimensions from the literature. The values of r_{max} in the constraint #1 used are 5, 7, and 12 for the mechanisms D, K, and C, respectively, derived from the existing dimensions (literature). To estimate a value of FTI_{min} for the constraint #5 in Sec. 2.1, we performed a single objective optimization of the mechanism, which maximized the critical FTI_{cr} for all three selected mechanisms. The existing mechanism dimensions from the literature were used as the initial guess for each case. The kinematic constraints #1–4,6 enlisted in Sec. 2.1 were enforced during the optimization using the patternsearch algorithm in MATLAB. The minimum (= 0.48) of these three critical FTI values was initially used for the FTI constraint for multiobjective optimization. During the multiobjective optimization, we observed that higher critical values are possible for all three mechanisms. We increased FTI_{min} to 0.65 for all mechanisms based on those observations. We faced another problem during the multiobjective optimization: it failed to find any feasible solution when we provided the existing mechanism dimensions as initial guesses (which did not satisfy constraints). To address this, we provided the solutions obtained from the single objective optimization as the initial feasible points for searching the Pareto set using the `paretosearch()` function in MATLAB.

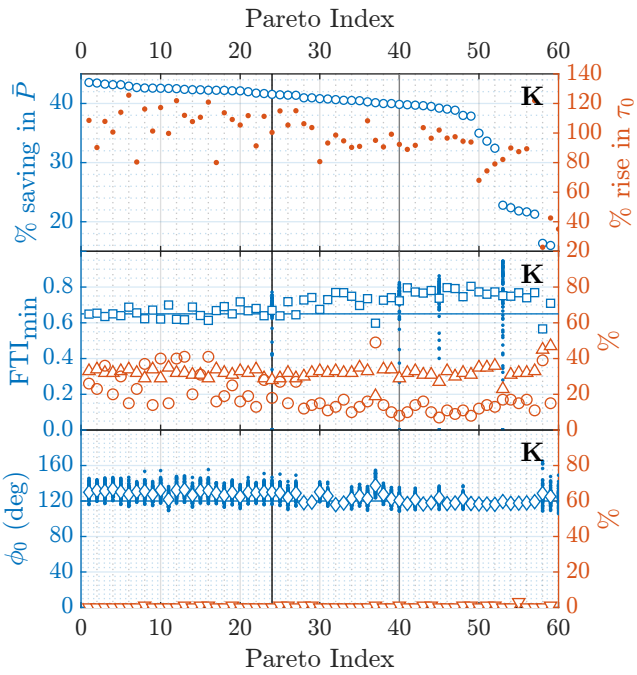
For the wing pitching velocity, we used the fruit fly kinematics data for all cases (Fig. 6). Since this work focuses on presenting a tool for optimization of the flapping mechanism (i.e., the sweeping velocity profile), any pitching velocity profile will serve the purpose of demonstration. However, while designing such an MAV, we would need to implement passive wing pitching kinematics in the present framework. We assumed $R = 22$ cm and $f = 15$ Hz, air density $\rho = 1.225 \times 10^{-3}$ g/cc, kinematic viscosity $\nu = 0.1568$ cm²/s, for all our computations.



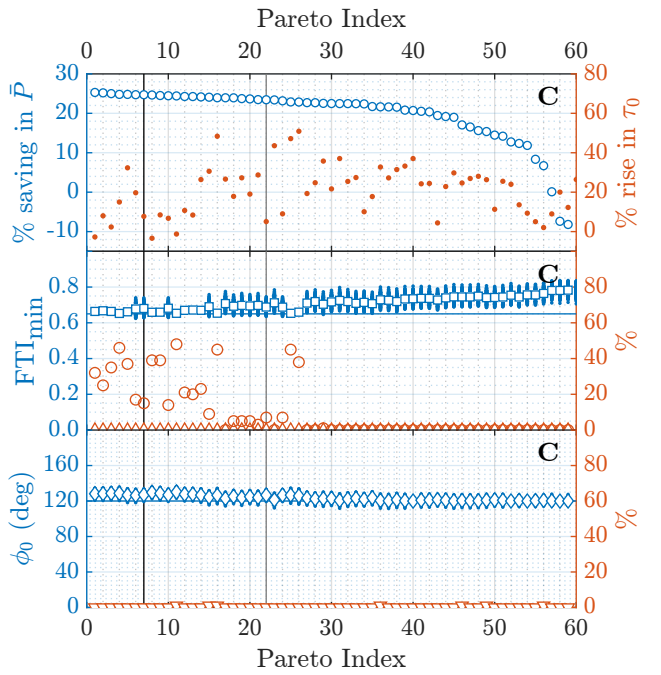
(a)



(b)



(c)



(d)

Figure 4: **(a)** Existing mechanisms above Pareto fronts for maximized mean lift (\bar{L}) and minimized mean power (\bar{P}) for topologies: D [12], K [13], C [14]. **Top rows of (b)–(d)**: Small variation among top 40–42 out of 60 Pareto solutions in percentage \bar{P} saving relative to the existing mechanisms for a given lift (blue circles). Manufacturing tolerance analysis: **Middle rows of (b)–(d)**: FTI_{\min} (blue dots) for 100 quasi-random linkages in ± 0.5 mm tolerance band of each Pareto solution. 10 to 50 linkages for topologies D and K and zero for topology C have singular configurations (triangles). Among non-singular ones, 5 to 50 for topologies D and K, and 0 to 50 for topology C violate FTI_{\min} constraint (red circles). Mean FTI_{\min} in tolerance band (squares) computed excluding singular linkages. **Bottom rows of (b)–(d)**: Amplitude (ϕ_0) (blue dots) for non-singular quasi-random linkages. Non-singular quasi-random linkages with amplitude < 100 deg are between 0 to 25 for topology D, and almost none for K and C (inverted triangles). Mean ϕ_0 in tolerance band (diamonds) computed excluding singular linkages and those with $\phi_0 < 100$ deg (relaxed from 120 deg limit). Refer Tab. 1 for the omitted Pareto solutions in the middle and bottom rows in (b)–(d). Gray dots in (a) – quasi-random linkages in the ± 0.5 mm tolerance band of the selected solution \square marked with black vertical lines in (b)–(d) (alternatives – gray vertical). Note: Gray dots exclude singular linkages and those with $\phi_0 < 100$ deg, with all other constraints relaxed due to minimal violation (non-critical).

Table 1: Criteria for rejection of a Pareto solution: Fig. 4(b),(c) and (d), middle rows: Pareto solutions for which (i) singularity or (ii) FTI violation percentage exceed the limits given below or (iii) mean $FTI_{\min} < 0.65$ (limit) were rejected, and not displayed in the plot. Note that singular quasi-random linkages were excluded while computing mean and FTI violation percentage. Fig. 4(b),(c) and (d), bottom rows: Pareto solutions for which amplitude–constraint violation percentage exceed the limit given below, or the mean amplitude of non-singular quasi-random linkages obeying relaxed amplitude constraint (100 deg), was lower than 120 deg (limit) were rejected, and not displayed in the plot. The limits are imposed to have a smaller set of Pareto solutions with low singularity percentage, low FTI_{\min} violation percentage, and low amplitude–constraint violation, from which final selection can be made based on mean power and peak-input torque values.

Mechanism	FTI_{\min} violation %	Singularity %	ϕ_0 constraint violation %
D	20	25	10
K	20	35	5
C	20	5	5

Table 2: Selected Pareto solutions: Marked with black vertical lines in Fig. 4 (b)–(d). Note: FTI_{\min} and ϕ_0 violation percentages are calculated after excluding the singular linkages from the tolerance band. The non-singular quasi-random linkages satisfying the relaxed amplitude constraint (100 deg) were simulated using 2D-UVLM to obtain mean lift and power (Fig. 4(a): gray dots). From that data, mean power decrease % and peak-input torque increase % were compared with the selected Pareto solution and reported here. A higher tolerance of ± 0.15 mm was simulated additionally for Mechanism D.

Mechanism	Tolerance (mm)	FTI_{\min} violation %	Singularity %	ϕ_0 constraint violation %	\bar{P} decrease %	τ_0 increase %
D	± 0.5	7	14	8	37^{+5}_{-10}	58^{+22}_{-26}
D	± 0.15	1	0	0	37^{+3}_{-4}	58^{+15}_{-9}
K	± 0.5	18	28	0	42^{+9}_{-7}	100^{+15}_{-37}
C	± 0.5	15	0	0	25^{+1}_{-10}	8^{+24}_{-12}

Further, for the fruit fly wing planform, $r_a = 3.7425$, $\hat{r}_2^2 = 0.345$, $\hat{r}_3^3 = 0.242$. The choice of these parameters should not affect the comparisons made between the different mechanisms.

For the finite element simulations, we used $K_{in} = 1$, $K_{out} = K_{tern} = 10^8$, and $G = 10^9$. The spring attached to the input link is soft. When we lock the mechanism to compute MA, we use a highly stiff spring at the output link. The axial stiffness of truss elements is set to high to simulate their rigid nature. The stiffnesses of springs attached to all other links are set to zero. Note that the units are not mentioned here. Here, only the relative values of these parameters matter because we are concerned only with the nondimensional outputs (output link angles and FTI) from the finite element simulations.

3.2 Optimization results

The Pareto fronts for the three mechanism topologies were obtained for a flapping frequency of 15 Hz (Fig. 4(a): blue dots). We observed that when we altered the frequency to meet a specific lift requirement, the mean power consumption did not vary much for 40 out of 60 Pareto points (Fig. 4(b), (c),(d): top rows). Therefore, we considered additional criteria for picking one for an MAV design rather than just choosing the one with the highest power savings. The mean power consumption and peak torque requirements are essential to select actuators such as brushless motors with added gearboxes. We must ensure that the selected mechanism leads to high mean power savings and low peak-input torque raises. The manufacturing tolerances could also adversely impact the mechanism’s performance. Therefore, we con-

ducted an uncertainty analysis of the mechanisms.

Additive manufacturing, such as fused deposition molding (FDM), is a common method for 3D printing of flapping wing MAV parts. FDM’s tolerance ranges between ± 0.2 and ± 0.5 mm. We chose the upper limit ± 0.5 mm to analyze the uncertainty in link-lengths from FDM. Assuming a crank-length of 10 mm for all mechanisms, we generated a set of 100 linkages from a selected Pareto solution using 100 quasi-random points (\mathbf{x} in Eqs. 13: l and \angle denote respectively, the link length and included angle between respective nodes numbered in subscripts: Fig. 1) using the Sobol sequence [38]. The Sobol sequence is regarded as the best method to generate quasi-random numbers, which perform significantly better than pseudo-random numbers in uncertainty analysis due to faster convergence and even coverage of the domain space.

$$\begin{aligned}
 D : \mathbf{x} &= \{l_{12}, l_{23}, l_{34}, l_{41}, l_{45}, l_{56}, l_{67}, l_{74}, l_{71}, \angle_{345}\} \\
 K : \mathbf{x} &= \{l_{12}, l_{23}, x_3, x_4, l_{41}, l_{45}, l_{56}, l_{67}, l_{74}, l_{71}, \angle_{345}\} \\
 C : \mathbf{x} &= \{l_{12}, l_{23}, l_{34}, l_{41}, l_{45}, l_{64}, l_{61}, \angle_{345}\} \quad (13)
 \end{aligned}$$

Post-generation, we analyzed the linkages in the tolerance band for the critical constraint violations – quick return ratio, Grashoff’s condition, amplitude, and FTI (singularity). The box constraints were not violated much to cause concern due to small link-length changes. The quick return ratio (QRR) remained in the 1 ± 0.02 range for all three mechanisms, D, K, and C, in their tolerance bands. Grashoff’s condition was satisfied by all 100 linkages in the bands for each of the three mechanisms due to the offset value 0.4 used in the optimization. The ampli-

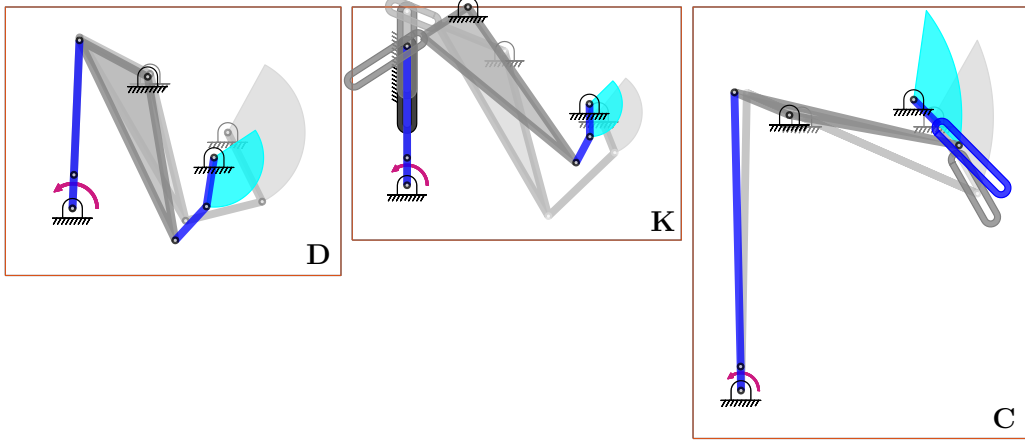


Figure 5: Selected optimal mechanisms compared with the existing mechanisms (shown in lighter gray shade): topologies: D - Deng et al. [12], K - Karásek et al. [13], C - Coleman et al. [14].

Table 3: Comparison between existing mechanisms and the selected Pareto solutions listed in Tab. 2: Differences lie in either the sweeping amplitude ϕ_0 or the mean lift coefficient \bar{C}_L . Flapping frequencies, mean power, and peak-input torque are listed for generating 100 gf of lift from the mechanisms. The selected Pareto solutions consume significantly lower power and operate at lower frequencies.

	existing					selected Pareto point				
	\bar{C}_L	ϕ_0	f	\bar{P}	τ_0	\bar{C}_L	ϕ_0	f	\bar{P}	τ_0
units	-	deg	Hz	W	kg.cm	-	deg	Hz	W	kg.cm
D	2.16	125	13.4	15.1	8.4	3.28	132	10.3	9.5	13.3
K	1.99	120	14.6	14.7	6.7	3.38	134	10.0	8.6	13.5
C	2.45	121	13.0	12.7	5.8	3.19	127	10.9	9.6	6.2

tude ϕ_0 and FTI_{\min} values for the quasi-random linkages in the tolerance bands of all Pareto solutions are shown in Fig 4 (b), (c) and (d) (middle and bottom rows). We found that the singularity percentage, i.e., the number of quasi-random linkages having singular configurations out of the 100, hovered between 10 to 50 for the mechanisms D and K and zero for the mechanism C. The number of non-singular quasi-random linkages violating the FTI_{\min} constraint lied between 5 to 50 for mechanisms D and K, and 0 to 50 for mechanism C. Further, the number of non-singular quasi-random linkages violating the relaxed amplitude constraint (<100 deg) lied between 0 to 25 for mechanism D, whereas it was close to zero for the other two mechanisms. Given these high values in some cases, we imposed maximum limits (Tab. 1) to get a smaller set of Pareto solutions from which final selections were made based on mean power and peak-input torque values (Tab. 2). We simulated these selected mechanisms using the 2D-UVLM to compare their mean lift and mean power values with those on the Pareto front (Fig. 4(a): gray dots). As a result, we found a significant variation in mean power savings for a given lift (Tab. 2) among the feasible quasi-random linkages, indicating that the chosen tolerance value of ± 0.5 mm is too large, and we must employ other fabrication methods that can offer high manufacturing tolerance. We simulated the selected Pareto solution for mechanism D in the ± 0.15 mm

tolerance band. The constraint violation and singularity percentage dropped significantly (Tab. 2: row 2). The range of mean power savings and peak-input torque increase were significantly lowered, thus increasing the reliability of the prototype upon fabrication.

The selected Pareto optimal flapping mechanisms are shown in Fig. 5 overlapped with the existing mechanisms in literature. Comparison of the existing mechanisms with the selected Pareto solutions shows that the optimized ones have amplitudes slightly higher, lift-coefficients significantly higher, and need lower frequencies to generate the same lift (Tab. 3), consuming 25–42% less power (Tab. 2), but requiring higher peak-input torques. The sweeping velocity profiles for the selected Pareto solutions are all asymmetric, unlike those for the existing mechanisms (Fig. 6).

4 Discussion

Rigid link flapping mechanisms are still the most practical choice for flapping wing MAVs to carry a useful payload and an onboard battery for free flight due to their long-term durability and reliability. While designing a flapping wing MAV with such mechanisms for high agility, maneuverability, and hovering ability like insects, it is crucial to reduce its weight as much as possible. One way to achieve that is by using single-DOF planar rigid

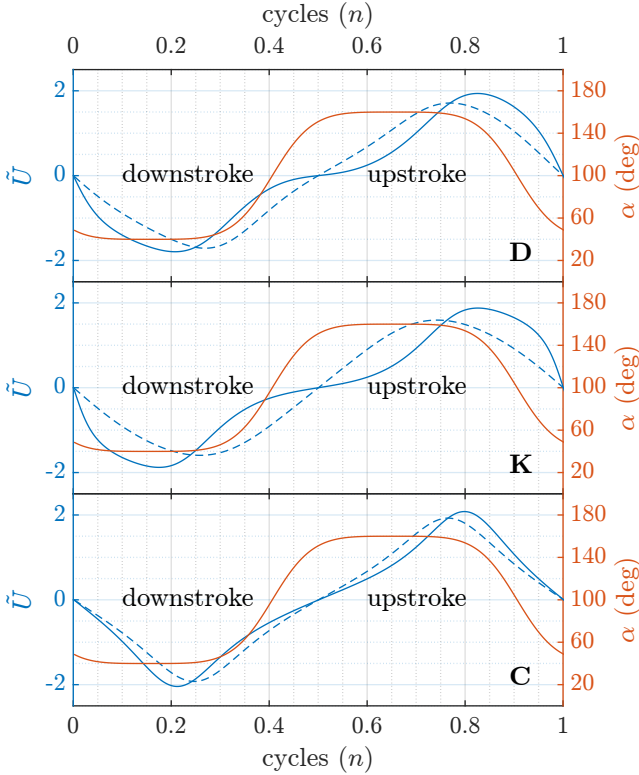


Figure 6: Nondimensional sweeping velocity \tilde{U} generated by the existing mechanisms in dotted, selected Pareto optimal mechanisms in dark blue: topologies used: D - Deng et al. [12], K - Karásek et al. [13], C - Coleman et al. [14]: Velocities are not symmetric about the midstroke position ($n = 0.25, 0.75$). The wing pitching angle α is shown in red. Corresponding lift coefficients are shown in the supplementary material.

linkages to generate the sweeping component of the flapping motion and optimizing its amplitude and the output link velocity profile for high lift and low power, such that smaller (and lesser) motors and batteries can be used. Existing rigid link flapping mechanisms are rarely optimized by computing lift and power in situ, and rather focus on replicating predefined amplitude and sinusoidal velocity profiles, both of which need not be optimal as shown in this study. The suboptimal selection of components for these MAVs is evident from short flight durations and motor failure due to overheating. The present work addresses these issues by combining a mechanism simulator with an aerodynamic analysis tool in a single optimization routine, thereby (i) optimizing the flapping mechanisms and (ii) providing a computational tool for the optimal selection of the MAV components. The mechanism simulator can analyze any generic planar single-DOF rigid link mechanism except for inclined sliders.

4.1 Optimization of flapping mechanisms

We optimized one-DOF planar rigid-link flapping mechanisms for high mean lift and low mean power consumption for a given flapping frequency and wing morphology. We observed from the study of three mechanism topologies that following the above procedure can achieve significant power saving (25–42%). We also saw that improvements in mechanisms are not necessarily from an increase in flapping amplitude but also from improved

sweeping velocity profiles generated by the mechanisms. The asymmetric sweeping velocity profiles from the optimal mechanisms show that assuming a symmetric velocity profile a priori is not justified. We also performed uncertainty analysis due to manufacturing tolerances, revealing that 3D printing using FDM may not be a suitable method for fabrication due to the low tolerances available (± 0.5 mm). With that, the tolerance band's worst-case would result in 16% more power consumption than the corresponding Pareto solution for the same lift. When we reduced tolerance in the range of CNC machining (± 0.15 mm), the worst case required only 5%

We observed that different mechanism topologies require varied power and peak input torques for a given design mean lift value. This trend suggests that the presented method can be combined with an optimization routine to obtain optimal topology for the flapping mechanism since the nonlinear finite element model can be used to analyze any generic planar rigid link mechanism of one DOF with binary and ternary links.

In the current approach, we fixed the flapping frequency f , wing size R , wing shape (fruit fly), and pitching angle profile $\alpha(t)$ and optimized the flapping mechanism dimensions. Wing shape and size are independent of the mechanism. Therefore, fixing them beforehand is justified. We assume $\alpha(t)$ to demonstrate the usefulness of the optimization. Practically, such mechanisms are used with passive wing pitching kinematics, which means $\alpha(t)$ depends on the sweeping velocity $\Omega(t)$ and the torsional stiffness of the joint of the wing-root with the fuselage. Therefore, including its formulation in the future should increase the applicability of the presented methodology for the flapping wing MAVs. Now, one may ask: is fixing the flapping frequency f a priori justified? During the optimization, the lift \bar{L} and power \bar{P} vary due to changes in the sweeping amplitude ϕ_0 and the lift coefficient C_L , due to changes in the link lengths. While varying f in a small range (10-20 Hz) we assumed the mean lift coefficient constant. This assumption is based on the observation that \bar{C}_L varies very little in this frequency range (supplementary material). With this assumption, we can say from Eqs. (10) and (12) that:

$$\bar{L} = cf^2, \quad \bar{P} = df^3 \quad (14)$$

where, c and d are proportionality constants independent of f . Therefore, compared to a reference mechanism (say, the existing one) with lift and power values \bar{L}_r and \bar{P}_r respectively at frequency f_r , a Pareto solution with the same lift \bar{L}_r at a different frequency f , will consume power \bar{P} given by:

$$\frac{\bar{P}}{\bar{P}_r} = \frac{d}{d_r} \left(\frac{c_r}{c} \right)^{3/2} \quad (15)$$

c , d , c_r , d_r are the respectively proportionality constants. The above equation implies that the power ratio is independent of the flapping frequency f_r , and thus has the same value for any lift L_r . Thus, provided all mechanisms generate the same lift, a mechanism that is $x\%$ better than the reference mechanism for that lift will always be $x\%$ better for every other lift. It means the mechanism that consumes the least power for that lift will consume the least power for every other lift L_r , i.e., for every

other frequency f_r . Therefore, allowing the lift to vary in the multi-objective optimization while keeping f unchanged is equivalent to having a constant lift and allowing f to vary freely. This result holds as long as \bar{C}_L does not vary much with f in the range considered. In the case of MAV with passive wing pitching, the pitching angle profile (i.e., the angle of attack) may depend on the flapping frequency. Therefore, the mean lift coefficient \bar{C}_L may depend significantly on the frequency f , implying that the power ratio with respect to the reference mechanism may no longer be independent of the lift value. In that case, we must allow f to vary during the optimization to obtain a lift vs power Pareto front similar to this study. The post-optimization analysis by varying the flapping frequency would no longer be valid, and we would select the Pareto point with the lift nearest to the design lift value.

4.2 Optimal selection of components for MAV design

Among MAVs with large amplitude 1-DOF rigid-link planar flapping mechanisms, only the Colibri by Roshanbin et al. [39] based on the mechanism by Karásek et al. [13], and the Robotic Hummingbird by Coleman et al. [14] were tested for free flight. Colibri with 160 mAh battery sustained flight for 15-20 s, while Robotic Hummingbird with 180 mAh battery lasted for 50-60 s until motors overheated. These flight times are insufficient for practical purposes. Bigger, heavier batteries need to be incorporated for longer runtime. However, the increased weight implies that we must reconsider many design aspects, such as the wing size, flapping frequency, and motor power rating. An improperly chosen motor cannot supply the required power without overheating or can be overpowered and heavy, rendering the design suboptimal. Since there are many parameters to consider, it is essential to have a computational tool to help find their optimal combination. The tool would reduce trial and error and experiments. The information from the present analysis can help in this regard.

Given the payload and flight time requirements, we can perform a preliminary selection of motors, batteries, wing size, and flapping frequency and estimate the overall weight and lift requirement. We can compute the power and peak-input torque requirements for this lift for the selected mechanism. If the selected motors are overpowered or underpowered, we iterate by choosing a different motor. If the estimated flight time from the power requirement is insufficient, we choose a bigger battery. Then, we have a revised weight estimate and lift requirement estimate. We reiterate this selection procedure until the requirements are met. The peak-input torque information also helps choose an appropriate gear ratio for the selected motor. In Tab. 3, we notice that the peak input torque increases in the case of the selected Pareto solution for all three mechanism topologies. It implies that a higher gear ratio would be needed in such a case. This increased gear ratio would result in some power loss due to gear friction and noise. These losses are not accounted for in this study.

4.3 Comments on choices and assumptions

In this analysis, we have excluded the inertial power consumption due to the mechanism for which a detailed CAD design would be required. The design must also be structurally optimized for deflection, fatigue, and stress failures. To include a crude estimate, we may increase the lift requirement by a factor (of safety). Deng et al. [12] noticed during their experiments that the mechanism alone consumes 0.13 W at 20 Hz when used without the wing onboard. However, to generate 27.8 gf of lift, the power consumption increased to 9.9 W. Therefore, the inertial power consumed by the mechanism is only a tiny fraction of the total power consumed. The above two reasons are sufficient to justify the exclusion of the inertial power computation of the mechanism.

In our analysis, we assumed both the revolute and sliding joints to be frictionless. If not properly lubricated, friction in sliding joints is expected to increase power consumption considerably compared to the revolute joints. Therefore, incorporating them would improve the accuracy of our analysis further.

We used a two-dimensional version of the extended UVLM for our computations, trading accuracy for computational speed. Efficient optimization with 3D analysis exploring better mechanism topologies is a part of future work.

5 Conclusion

A multiobjective optimization of one degree of freedom planar rigid link flapping mechanisms for maximum lift and minimum power consumption was performed. This tool provides a Pareto optimal set and the associated power, peak input torque, and lift values that can be used to optimally select actuators, gear ratio, and battery capacity to meet the required payload and flight time requirements from a flapping wing MAV with a given mechanism topology. We found that the optimization can achieve significant power savings (25–42%). The improvements in the mechanisms are not necessarily due to an increase in amplitude but also to an increase in mean lift coefficient, which happens due to asymmetric sweeping velocity profiles generated by the mechanisms. The uncertainty analysis showed the need for high manufacturing tolerances to achieve reliable performance. The procedure can also be used to compare different mechanism topologies. With further work, it can be used in optimizing mechanism topology, as we observed significant variation in power consumption and peak input torque values across different topologies for a given design lift value.

Acknowledgment

This work was supported by Visvesvaraya PhD Scheme, MEITY, Government Of India MEITY-PHD-2065.

A 2D-UVLM

In hovering flight, for a finite wing sweeping with angular velocity Ω , the translation speed at radial distance r from the rotation axis is $U = \Omega r$. The equations given here are non-dimensionalized to eliminate the effect of wing size and frequency. \tilde{a} denotes nondimensional a . When using the blade element theory, we use the following reference scales for a wing chord of length c at the radial distance r from the rotation axis:

$$\begin{aligned} L_{\text{ref}} &= c, & \Omega_{\text{ref}} &= 2\phi_0 f, & U_{\text{ref}} &= \Omega_{\text{ref}} r, \\ T_{\text{ref}} &= \frac{L_{\text{ref}}}{U_{\text{ref}}}, & \dot{\alpha}_{\text{ref}} &= \frac{1}{T_{\text{ref}}} \end{aligned}$$

where, ϕ_0 is the sweeping (flapping) amplitude, and f is the flapping frequency. We use the mean sweeping angular velocity as the scale Ω_{ref} for sweeping angular velocity. For wing pitching velocity $-\dot{\alpha}(t)$, we use $1/T_{\text{ref}}$ (can be verified from Eq. (16)) as the reference scale $\dot{\alpha}_{\text{ref}}$. As a consequence of the blade element theory, $r = r_2$ results in a suitable velocity reference scale $U_{\text{ref}} = \Omega_{\text{ref}} r_2$ for the entire wing, where r_2 is the second moment of wing area. In the case of flapping translation velocity in hovering, for different wing-sizes, force coefficients converge better [40] with this velocity reference $U_{\text{ref}} = 2\phi_0 f r_2$, than with wing-tip velocity $2\phi_0 f R$.

The impenetrability condition at the collocation point CP_j on j^{th} element ($j = 1, 2, \dots, N$):

$$\underbrace{(\tilde{\mathbf{u}}_j^{\text{b}} + \tilde{\mathbf{u}}_j^{\text{w}}) \cdot \hat{\mathbf{n}}_j}_{\text{flow velocity}} = \underbrace{\left[\tilde{\Omega} \hat{\mathbf{s}} - \tilde{\alpha} \hat{\mathbf{k}} \times (\tilde{\mathbf{r}}_j^{\text{CP}} - \tilde{\mathbf{r}}_0) \right] \cdot \hat{\mathbf{n}}_j}_{\text{chord-element velocity}} \quad (16)$$

where, $\tilde{\mathbf{u}}_j^{\text{b}}$ and $\tilde{\mathbf{u}}_j^{\text{w}}$ are the flow velocities due to all $N + 1$ bound and all N_{w} wake vortices at the collocation point CP_j with position $\tilde{\mathbf{r}}_j^{\text{CP}}$, given by Eqs. (17)–(18). $\hat{\mathbf{n}}_j$ is the normal to the wing chord at that point. $\hat{\mathbf{k}}$ is the normal to the plane x - y of the wing-chord. $\hat{\mathbf{s}}$ indicates the direction of the velocity U . This condition yields N equations in $N + 1$ unknowns $\Gamma_j^{\text{b}}, i = 1, 2, 3, \dots, (N + 1)$.

$$\tilde{\mathbf{u}}_j^{\text{b}} = \sum_{i=1}^{N+1} \frac{\tilde{\Gamma}_i^{\text{b}} \hat{\mathbf{k}} \times (\tilde{\mathbf{r}}_j^{\text{CP}} - \tilde{\mathbf{r}}_i^{\text{b}})}{2\pi \|\tilde{\mathbf{r}}_j^{\text{CP}} - \tilde{\mathbf{r}}_i^{\text{b}}\|^2} \quad (17)$$

$$\tilde{\mathbf{u}}_j^{\text{w}} = \sum_{i=1}^{N_{\text{w}}} \frac{\tilde{\Gamma}_i^{\text{w}} \hat{\mathbf{k}} \times (\tilde{\mathbf{r}}_j^{\text{CP}} - \tilde{\mathbf{r}}_i^{\text{w}})}{2\pi \|\tilde{\mathbf{r}}_j^{\text{CP}} - \tilde{\mathbf{r}}_i^{\text{w}}\|^2 + \tilde{r}_c^2} \quad (18)$$

Here, $\tilde{\mathbf{r}}_i^{\text{b}}$ and $\tilde{\mathbf{r}}_i^{\text{w}}$ are positions of bound vortices $\tilde{\Gamma}_i^{\text{b}}$ and wake vortices $\tilde{\Gamma}_i^{\text{w}}$ respectively. To model the viscous diffusion in wake vortices, a vortex-core growth model proposed by Ramasamy et al. [41], which considers eddy viscosity and improves over the Lamb Oseen model, is used. The nondimensional core radius \tilde{r}_c is given by:

$$\tilde{r}_c^2 = 4\alpha_L \left(\frac{1}{Re} + a_1 \tilde{\Gamma}_i^{\text{w}} \right) \tilde{t}$$

where, α_L is the Lamb constant, a_1 is the Squire's parameter, ν is the kinematic viscosity of the medium, and \tilde{t} is the nondimensional time since vortex shedding. Reynolds

number in hovering flight

$$Re = \frac{U_{\text{ref}} L_{\text{ref}}}{\nu} = (2\phi_0 f R^2) \frac{\hat{f}_2}{r_a \nu}$$

where, \hat{f}_2 is the nondimensional second moment of the wing area, R is the distance of the wing-tip to the axis of wing revolution, r_a is the wing aspect ratio = R/\bar{c} , \bar{c} being the mean chord length.

The Kelvin circulation theorem yields the $(N + 1)^{\text{th}}$ equation

$$\sum_{j=1}^{N+1} \tilde{\Gamma}_j^{\text{b}} + \sum_{j=1}^{N_{\text{w}}} \tilde{\Gamma}_j^{\text{w}} = 0$$

The $N + 1$ equations are linear in $N + 1$ unknowns Γ_j^{b} and can be solved easily.

Using the unsteady Bernoulli equation in terms of the moving frame x - y [42]¹ attached to a thin flat wing-chord, the pressure coefficient difference $\Delta C_p = (p_1 - p_2)/(\frac{1}{2}\rho U_{\text{ref}}^2)$ at k^{th} time step t_k , for j^{th} element, can be computed at the collocation point CP_j as:

$$\begin{aligned} \Delta C_p &= 2 \left[\left(-\tilde{\Omega} \cos(\alpha + \beta) + \tilde{\mathbf{u}}_j^{\text{w}} \cdot \hat{\mathbf{x}} \right) \frac{\tilde{\Gamma}_{j,k}^{\text{b}}}{\tilde{d}} \right. \\ &\quad \left. + \sum_{i=1}^j \frac{\tilde{\Gamma}_{i,k}^{\text{b}} - \tilde{\Gamma}_{i,k-1}^{\text{b}}}{\tilde{t}_k - \tilde{t}_{k-1}} \right] \quad (19) \end{aligned}$$

where, \tilde{d} is element length, $\tilde{\Gamma}_{j,k}^{\text{b}}$ is the circulation of j^{th} bound vortex element at time \tilde{t}_k . Sides 1 and 2 of the chord are shown in Fig. 3c; 2 corresponds to the negative y half-plane.

The pressure-force coefficient \mathbf{C}_F on the wing-chord, with magnitude C_F :

$$\begin{aligned} \mathbf{C}_F &= -\hat{\mathbf{y}} \sum_{j=1}^N \Delta C_p \tilde{d} \\ &= C_F (-\sin \alpha \hat{\boldsymbol{\phi}} + \cos \alpha \hat{\boldsymbol{Z}}) \quad (20) \end{aligned}$$

Thus, lift coefficient i.e., the vertical component:

$$C_L = C_F \cos \alpha$$

And, the horizontal component:

$$C_H = -C_F \sin \alpha$$

Conventionally, drag is the force opposite to the motion. Hence, the drag coefficient is:

$$C_D = -\text{sign}(U) C_H$$

References

- [1] Song, F., Yan, Y., and Sun, J., 2023, "Review of insect-inspired wing micro air vehicle," *Arthropod Structure and Development*, **72**, p. 101225.
- [2] Singh, S., Zuber, M., Hamidon, M. N., Mazlan, N., Basri, A. A., and Ahmad, K. A., 2022, "Classification of actuation mechanism designs with structural block diagrams for flapping-wing drones: A comprehensive review," *Progress in Aerospace Sciences*, **132**.

¹Sec. 3.61 of the book

- [3] Yousaf, R., Shahzad, A., Qadri, M. M., and Javed, A., 2021, "Recent advancements in flapping mechanism and wing design of micro aerial vehicles," *Proceedings of the Institution of Mechanical Engineers, Part C: Journal of Mechanical Engineering Science*, **235**, pp. 4425–4446.
- [4] Bergou, A. J., Xu, S., and Wang, Z. J., 2007, "Passive wing pitch reversal in insect flight," *Journal of Fluid Mechanics*, **591**, pp. 321–337.
- [5] Whitney, J. P. and Wood, R. J., 2010, "Aeromechanics of passive rotation in flapping flight," *Journal of Fluid Mechanics*, **660**, pp. 197–220.
- [6] Hu, F. and Liu, X., 2019, "Effects of stroke deviation on hovering aerodynamic performance of flapping wings," *Physics of Fluids*, **31**, p. 111901.
- [7] Luo, G., Du, G., and Sun, M., 2018, "Effects of stroke deviation on aerodynamic force production of a flapping wing," *AIAA Journal*, **56**, pp. 25–35.
- [8] Sane, S. P. and Dickinson, M. H., 2001, "The control of flight force by a flapping wing: lift and drag production," *Journal of Experimental Biology*, **204**, pp. 2607–2626.
- [9] Wang, C., Zhou, C., and Xie, P., 2016, "Numerical investigation into the effects of stroke trajectory on the aerodynamic performance of insect hovering flight," *Journal of Mechanical Science and Technology*, **30**, pp. 1659–1669.
- [10] Zhang, H., Wen, C., and Yang, A., 2016, "Optimization of lift force for a bio-inspired flapping wing model in hovering flight," *International Journal of Micro Air Vehicles*, **8**, pp. 92–108.
- [11] Phan, H. V., Truong, Q. T., and Park, H. C., 2019, "Extremely large sweep amplitude enables high wing loading in giant hovering insects," *Bioinspiration and Biomimetics*, **14**, p. 066006.
- [12] Deng, H., Xiao, S., Huang, B., Yang, L., Xiang, X., and Ding, X., 2021, "Design optimization and experimental study of a novel mechanism for a hover-able bionic flapping-wing micro air vehicle," *Bioinspiration and Biomimetics*, **16**.
- [13] Karásek, M., Hua, A., Nan, Y., Lalami, M., and Preumont, A., 2014, "Pitch and roll control mechanism for a hovering flapping wing MAV," *International Journal of Micro Air Vehicles*, **6**, pp. 253–264.
- [14] Coleman, D., Benedict, M., Hirshikeshaven, V., and Chopra, I., 2017, "Development of a robotic hummingbird capable of controlled hover," *Journal of the American Helicopter Society*, **62**.
- [15] Jeon, J. H., Cho, H., Kim, Y., Lee, J. H., Gong, D. H., Shin, S. J., and Kim, C., 2017, "Design and analysis of the link mechanism for the flapping wing MAV using flexible multi-body dynamic analysis," *International Journal of Micro Air Vehicles*, **9**, pp. 253–269.
- [16] Lin, C.-C. and Chang, W.-T., 2002, "The force transmissivity index of planar linkage mechanisms," *Mechanism and Machine Theory*, **37**(12), pp. 1465–1485.
- [17] Berman, G. J. and Wang, Z. J., 2007, "Energy-minimizing kinematics in hovering insect flight," *Journal of Fluid Mechanics*, **582**, pp. 153–168.
- [18] Nabawy, M. R. and Crowther, W. J., 2015, "Aero-optimum hovering kinematics," *Bioinspiration and Biomimetics*, **10**, p. 044002.
- [19] Yan, Z., Taha, H. E., and Hajj, M. R., 2015, "Effects of aerodynamic modeling on the optimal wing kinematics for hovering MAVs," *Aerospace Science and Technology*, **45**, pp. 39–49.
- [20] Ke, X., Zhang, W., Cai, X., and Chen, W., 2017, "Wing geometry and kinematic parameters optimization of flapping wing hovering flight for minimum energy," *Aerospace Science and Technology*, **64**, pp. 192–203.
- [21] Nguyen, A. T., Tran, N. D., Vu, T. T., Pham, T. D., Vu, Q. T., and Han, J. H., 2019, "A Neural-network-based Approach to Study the Energy-optimal Hovering Wing Kinematics of a Bionic Hawkmoth Model," *Journal of Bionic Engineering*, **16**, pp. 904–915.
- [22] Bhat, S. S., Zhao, J., Sheridan, J., Hourigan, K., and Thompson, M. C., 2020, "Effects of flapping-motion profiles on insect-wing aerodynamics," *Journal of Fluid Mechanics*, **884**, p. A8.
- [23] Lang, X., Song, B., Yang, W., Yang, X., and Xue, D., 2023, "Sensitivity Analysis of Wing Geometric and Kinematic Parameters for the Aerodynamic Performance of Hovering Flapping Wing," *Aerospace 2023*, Vol. 10, Page 74, **10**, p. 74.
- [24] Terze, Z., Pandža, V., Kasalo, M., and Zlatar, D., 2021, "Optimized flapping wing dynamics via DMOC approach," *Nonlinear Dynamics*, **103**, pp. 399–417.
- [25] Sun, M. and Tang, J., 2002, "Lift and power requirements of hovering flight in *Drosophila virilis*," *Journal of Experimental Biology*, **205**(16), pp. 2413–2427.
- [26] Huang, M., 2019, "Optimization of flapping wing mechanism of bionic eagle," *Proceedings of the Institution of Mechanical Engineers, Part G: Journal of Aerospace Engineering*, **233**(9), pp. 3260–3272.
- [27] Han, Y.-J., Yang, H.-H., and Han, J.-H., 2023, "Twist-Coupled Flapping Mechanism for Bird-Type Flapping-Wing Air Vehicles," *Journal of Mechanisms and Robotics*, **15**(5), p. 051017.
- [28] Nguyen, A. T., Kim, J. K., Han, J. S., and Han, J. H., 2016, "Extended unsteady vortex-lattice method for insect flapping wings," *Journal of Aircraft*, **53**, pp. 1709–1718.
- [29] Rai, A. K., Saxena, A., and Mankame, N. D., 2010, "Unified synthesis of compact planar path-generating linkages with rigid and deformable members," *Structural and Multidisciplinary Optimization*, **41**, pp. 863–879.
- [30] Dickinson, M. H., Lehmann, F. O., and Sane, S. P., 1999, "Wing rotation and the aerodynamic basis of insect flight," *Science*, **284**, pp. 1954–1960.
- [31] Persson, P.-O., Willis, D., and Peraire, J., 2012, "Numerical simulation of flapping wings using a panel method and a high-order Navier–Stokes solver," *International Journal for Numerical Methods in Engineering*, **89**(10), pp. 1296–1316.
- [32] Ansari, S. A., Żbikowski, R., and Knowles, K., 2006, "Non-linear unsteady aerodynamic model for insect-like flapping wings in the hover. Part 1: Methodology and analysis," *Proceedings of the Institution of Mechanical Engineers, Part G: Journal of Aerospace Engineering*, **220**(2), pp. 61–83.
- [33] Ansari, S. A., Żbikowski, R., and Knowles, K., 2006, "Non-linear unsteady aerodynamic model for insect-like flapping wings in the hover. Part 2: Implementation and validation," *Proceedings of the Institution of Mechanical Engineers, Part G: Journal of Aerospace Engineering*, **220**(3), pp. 169–186.
- [34] Rocca, B. A., Preidikman, S., Massa, J. C., and Mook, D. T., 2013, "Modified unsteady vortex-lattice method to study flapping wings in hover flight," *AIAA Journal*, **51**, pp. 2628–2642.
- [35] Wang, Z. J., Birch, J. M., and Dickinson, M. H., 2004, "Unsteady forces and flows in low Reynolds number hovering flight: two-dimensional computations vs robotic wing experiments," *Journal of Experimental Biology*, **207**(3), pp. 449–460.
- [36] Katz, J. and Plotkin, A., 2001, *Low-speed aerodynamics*, Vol. 13, Cambridge university press.
- [37] Polhamus, E. C., 1971, "Predictions of vortex-lift characteristics by a leading-edge suction analogy," *Journal of Aircraft*, **8**(4), pp. 193–199.
- [38] Cao, Y., Yan, H., Liu, T., and Yang, J., 2016, "Application of Quasi-Monte Carlo Method Based on Good Point Set in Tolerance Analysis," *Journal of Computing and Information Science in Engineering*, **16**(2), p. 021008.
- [39] Roshanbin, A., Altartouri, H., Karásek, M., and Preumont, A., 2017, "COLIBRI: A hovering flapping twin-wing robot," *International Journal of Micro Air Vehicles*, **9**(4), pp. 270–282.
- [40] Lua, K. B., Lim, T. T., and Yeo, K. S., 2014, "Scaling of Aerodynamic Forces of Three-Dimensional Flapping Wings," *AIAA Journal*, **52**(5), pp. 1095–1101.
- [41] Ramasamy, M. and Leishman, J. G., 2007, "A Reynolds Number Based Blade Tip Vortex Model," *Journal of the American Helicopter Society*, **52**, pp. 214–223.
- [42] 1956, "Theoretical hydrodynamics. By L. M. Milne-Thomson. London (Macmillan), 3rd Edition, 1955. Pp. xxi, 632; Figs.; Tables. 60s," *Quarterly Journal of the Royal Meteorological Society*, **82**(353), pp. 379–379.
- [43] Ghommam, M., Collier, N., Niemi, A. H., and Calo, V. M., 2014, "On the shape optimization of flapping wings and their performance analysis," *Aerospace Science and Technology*, **32**, pp. 274–292.
- [44] Minotti, F. O., 2002, "Unsteady two-dimensional theory of a flapping wing," *Physical Review E - Statistical Physics, Plasmas, Fluids, and Related Interdisciplinary Topics*, **66**, p. 10.

Supplement

S1 2D-UVLM Convergence and Validation

S1.1 Convergence study of 2D-UVLM

We varied the number of panels $N = 10, 20, 40, 60, 80$, and the nondimensional time step $\delta\tilde{t} = \frac{\tilde{d}/\tilde{\Omega}_{\max}}{N_t}$ with $N_t = 1, 2, 4, 6, 8$, on fruit fly wing kinematics data (Fig. S1). $N_t = 1$ yields the time for the lattice element to move by one element length \tilde{d} with velocity $\tilde{\Omega}_{\max}$. We found that N_t affects convergence significantly more than N , also observed by Ghommem et al. [43]. Among the 25 combinations of N and N_t , 9 converged with the mean variation in lift coefficient $\epsilon = \delta\bar{C}_L = 0.025$, for $N = 40, 60, 80$ and $N_t = 4, 6, 8$. The computation time for three flapping cycles, however, varied significantly from 13 min for $N = 40, N_t = 4$, 22 min for $N = 40, N_t = 6$ to 3 hr 6 min for $N = 80, N_t = 8$, on Ryzen 5600X processor with 32 GB DDR4 RAM, running MATLAB 2024a. To balance computation time with convergence, we chose $N = 40$ and $N_t = 4$ for all our simulations. We observed that for Squire's parameter $a = 10^{-4}$, convergence was achieved in all cases considered in this study.

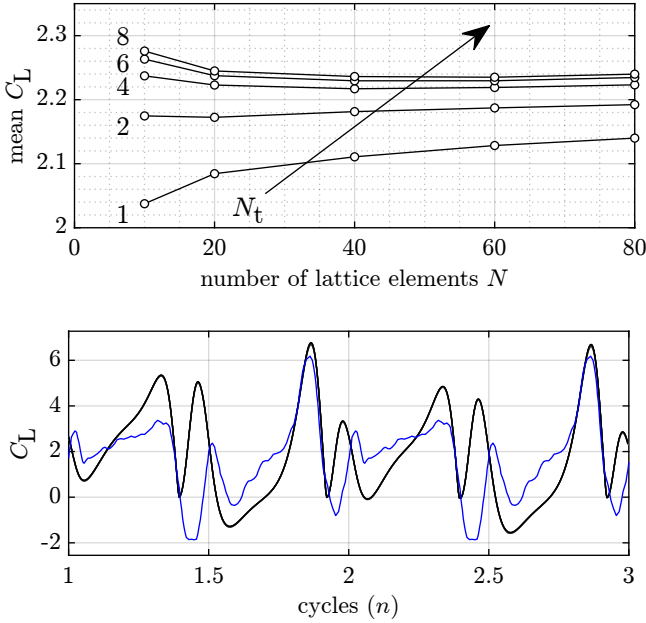


Figure S1: Convergence study of 2D UVLM: Computed lift coefficients C_L by varying number of lattice elements $N = 10, 20, 40, 60, 80$, and time step $\delta\tilde{t} = \frac{\tilde{d}/\tilde{\Omega}_{\max}}{N_t}$ with $N_t = 1, 2, 4, 6, 8$ using fruit fly wing kinematics data. (top) Each curve corresponds to a single value of N_t as labeled, whereas N increases from 10 to 80 in each curve towards right. With higher N_t ($= 4, 6, 8$), the variation in mean C_L is small with N , especially, for $N = 40, 60, 80$. Lift coefficients for these 9 combinations of N and N_t (bottom figure) almost overlap over each other, indicating convergence. The curve in blue color is the experimental data given by Dickinson et al. [30].

S1.2 Validation of 2D-UVLM against experimental data

Tables S1 and S2 compare the lift and drag coefficients computed from 2D-UVLM with those available from the experimental data in the literature. To perform these simulations, we used the wing kinematics functions given by Minotti [44] by interpolating the experimental data [8,30]. In some cases, the lift coefficients from 2D-UVLM are close to the experiments. But, the deviation is large in the case of drag coefficients. However, methods such as CFD that are more accurate are computationally costly to be of any use for optimization purposes. It led us to continue with the UVLM for our task. We noted that the power estimates would be underpredicted due to the negative deviation in drag coefficients. The variation of these coefficients during a flapping cycle is shown in Fig. S2.

Table S1: Comparison of lift coefficients computed from the 2D-UVLM with the experimental data available in literature.

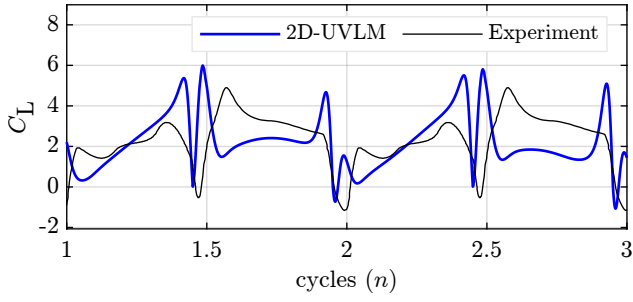
Case	Experiment \bar{C}_L	UVLM \bar{C}_L	Deviation %
Fruit fly [30]	1.75	2.00	14
Oval-A [8]	2.34	2.31	-1
Oval-B [8]	2.08	2.31	11
Figure 8-A [8]	2.59	2.14	-17
Figure 8-B [8]	1.87	2.25	21

Table S2: Comparison of drag coefficients computed from the 2D-UVLM with the experimental data available in literature.

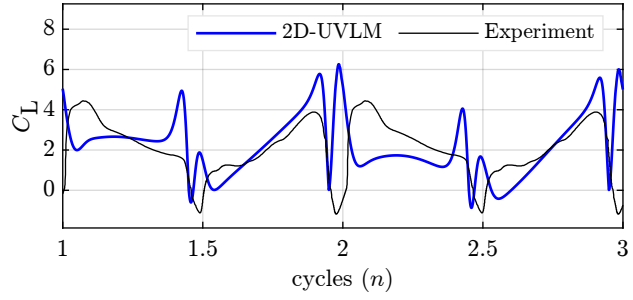
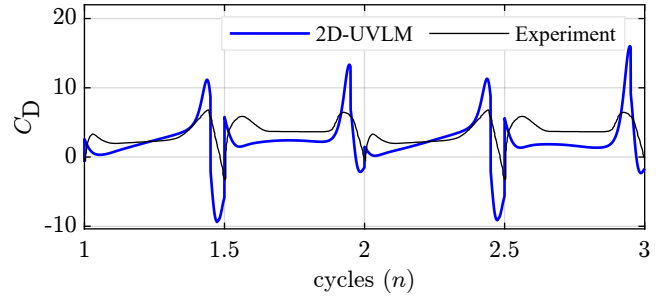
Case	Experiment \bar{C}_D	UVLM \bar{C}_D	Deviation %
Fruit fly [30]	2.86	1.59	-44
Oval-A [8]	3.48	2.27	-35
Oval-B [8]	3.03	2.20	-27
Figure 8-A [8]	3.13	2.61	-17
Figure 8-B [8]	3.22	1.40	-57

S1.3 Variation of lift and drag coefficients with flapping frequency

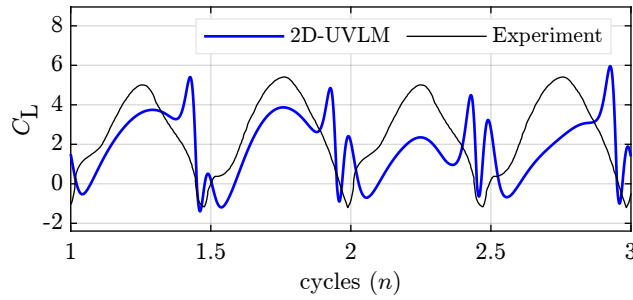
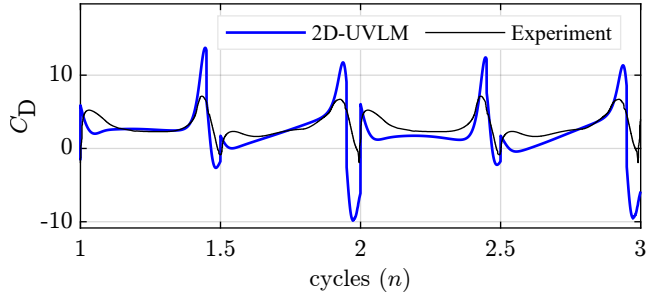
We varied the flapping frequency between 10–20 Hz, and computed mean lift and drag coefficients for different cases listed in Tab. S3. The wing-pitching angle profile for all cases was used from fruit fly wing kinematics [30]. The coefficients do not vary much, so we can assume them to be constant in that small range of the flapping frequency.



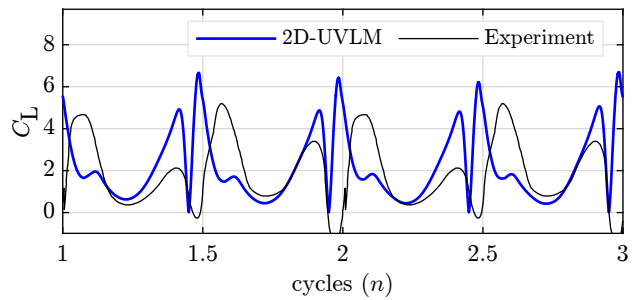
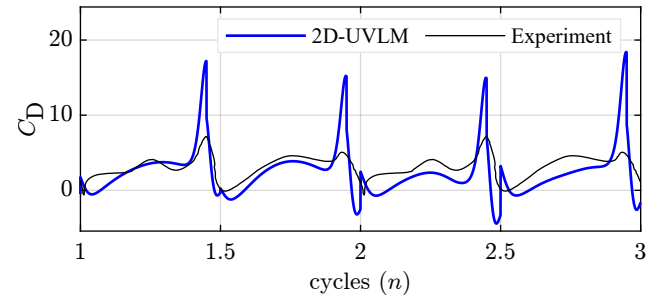
(a) Oval-A



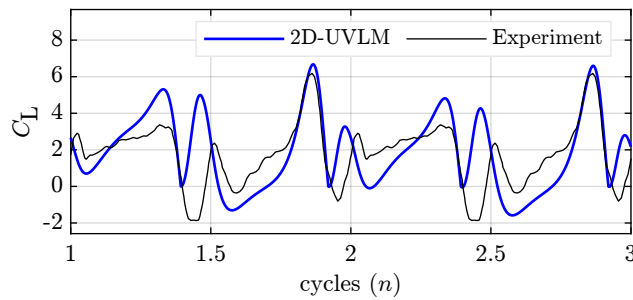
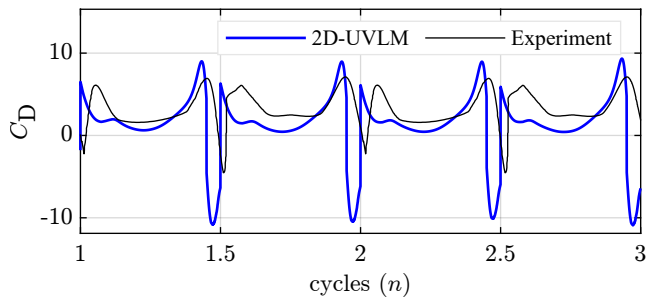
(b) Oval-B



(c) Figure of 8-A



(d) Figure of 8-B



(e) Fruit fly

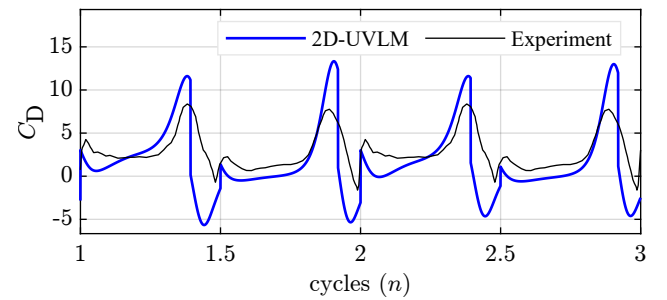


Figure S2: Lift and drag coefficients from 2D-UVLM (thick and blue) for oval, figure-8, and fruit fly flight patterns. Experimental data (thin and black) from oval and figure-8 patterns are taken from [8] and for fruit fly pattern from [30].

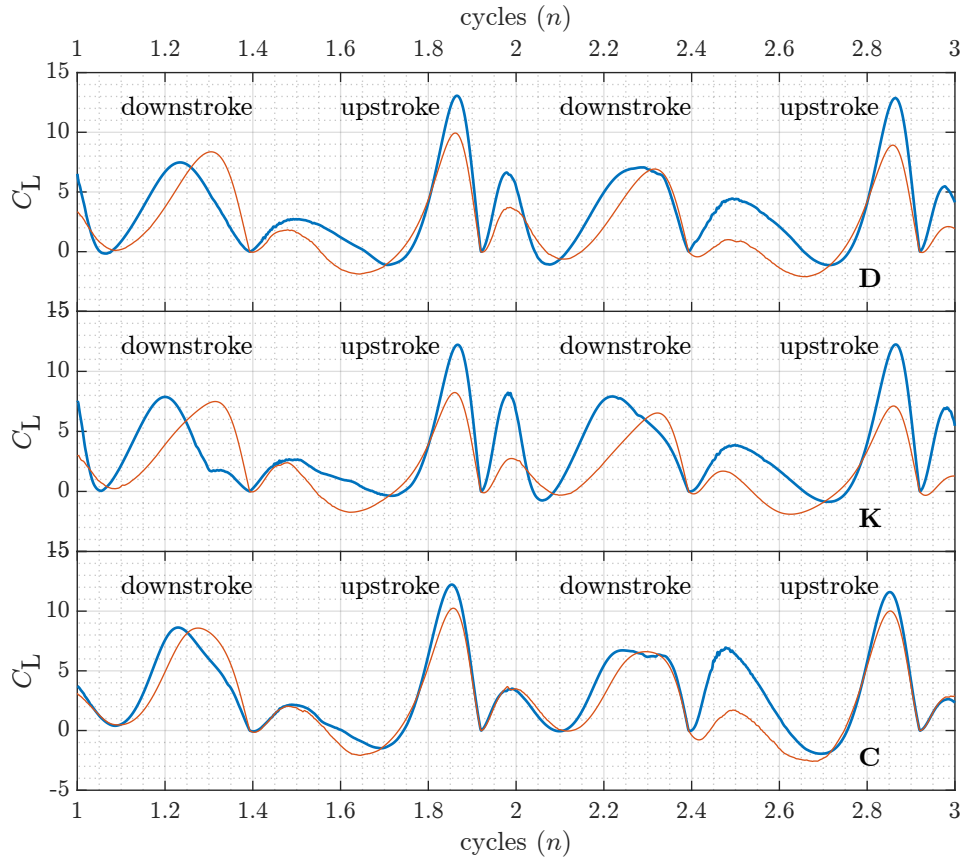


Figure S3: Lift coefficients C_L generated by the existing mechanisms in thin red; selected Pareto optimal mechanisms in thick blue: topologies used: D - Deng et al. [12], K - Karásek et al. [13], C - Coleman et al. [14]. The optimal mechanisms have smaller negative valleys during upstrokes. Peaks due to rotational effect (around $n = 1.9, 2.9$) during upstrokes are higher when sweeping velocities are higher than those of the existing mechanisms (Fig. 6). Peaks due to wing-wake interaction (around $n = 1.5, 2.5$) at the end of downstroke are higher. The optimal mechanisms sweep much slower around these times. During downstrokes, the lift develops faster coinciding with the faster acceleration of the optimal mechanisms in these periods (around $n = 1.3, 2.3$).

Table S3: Mean lift and drag coefficients for varied flapping frequencies.

		10 Hz	15 Hz	20 Hz
Fruit fly [30]	\bar{C}_L	1.780	1.779	1.774
	\bar{C}_D	1.513	1.509	1.502
Deng et al. [12]	\bar{C}_L	2.126	2.164	2.196
	\bar{C}_D	2.563	2.604	2.588
Karásek et al. [13]	\bar{C}_L	2.018	1.991	2.021
	\bar{C}_D	2.389	2.426	2.389
Coleman et al. [14]	\bar{C}_L	2.399	2.445	2.385
	\bar{C}_D	2.657	2.673	2.675